On the Development and Demise of the Fall 2019 Southeast U.S. Flash Drought: Links to an Extreme Positive IOD

SIEGFRIED D. SCHUBERT,[a,b] YEHUI CHANG,[a,c] ANTHONY M. DEANGELIS,[b] HAILAN WANG,[d] AND RANDAL D. KOSTER[a]

[a] *Global Modeling and Assimilation Office, NASA GSFC, Greenbelt, Maryland*
[b] *Science Systems and Applications, Inc., Lanham, Maryland*
[c] *Morgan State University, Baltimore, Maryland*
[d] *Climate Prediction Center, NCEP/NWS/NOAA, College Park, Maryland*

(Manuscript received 9 June 2020, in final form 23 November 2020)

ABSTRACT: Much of the southeast United States experienced record dry conditions during September of 2019, with the area in abnormally dry to exceptional drought conditions growing from 25% at the beginning of the month to 80% by the end of the month. The drought ended just as abruptly due to above-normal rain that fell during the second half of October. In this study we employed MERRA-2 and the GEOS-5 AGCM to diagnose the underlying causes of the drought's onset, maintenance, and demise. The basic approach involves performing a series of AGCM simulations in which the model is constrained to remain close to MERRA-2 over prespecified areas that are external to the drought region. The start of the drought appears to have been forced by anomalous heating in the central/western tropical Pacific that resulted in low-level anticyclonic flow and a tendency for descending motion over much of the Southeast. An anomalous ridge associated with a Rossby wave train (emanating from the Indian Ocean region) is found to be the main source of the most intense temperature and precipitation anomalies that develop over the Southeast during the last week of September. A second Rossby wave train (emanating from the same region) is responsible for the substantial rain that fell during the second half of October to end the drought. The links to the Indian Ocean dipole (with record positive values) as well as a waning El Niño allow some speculation as to the likelihood of similar events occurring in the future.

KEYWORDS: Rossby waves; Teleconnections; Drought; Extreme events

1. Introduction

The United States experienced extreme dry conditions throughout much of the Southeast during September and early October of 2019, characterized by record or near record-breaking heat and precipitation deficits. The drought developed rapidly, with the area in abnormally dry to exceptional drought conditions (D0–D3, as defined by the U.S. Drought Monitor) growing from 25% at the beginning of the month to 80% by the end of the month.[1] In fact, Mississippi, Alabama, Georgia, Florida, Kentucky, and West Virginia had their driest Septembers on record over the period 1895–2019 (with Tennessee, Virginia, Maryland, Delaware, and New Jersey having the second driest). Only the Carolinas were spared substantial drought conditions, as a result of the copious amount of rain produced by Hurricane Dorian as it moved up the Atlantic coast in early September. Above-normal rainfall during the second half of October did much to alleviate the drought so that by the end of November, the area of the southeastern United States (SEUS) experiencing drought conditions differed little from that in early September.[2]

This study investigates the underlying causes of the drought and its recovery. Previous studies of North American drought have highlighted the important, but overall modest, impact of SST-forced teleconnections (e.g., Seager and Hoerling 2014), although much of that impact occurs on seasonal and longer time scales, with tropical Pacific SST playing the dominant role. Atlantic SST also appears to play a role, especially in forcing multiyear and decadal-time-scale droughts in the Great Plains (e.g., Nigam et al. 2011). The origins of shorter-term (subseasonal) droughts such as the flash drought examined here are less clear, although there is mounting evidence that subseasonal atmospheric teleconnections such as those associated with atmospheric Rossby waves (e.g., Schubert et al. 2011; Wang et al. 2014; DeAngelis et al. 2020) may be important, with land feedbacks possibly acting to prolong or amplify the drought-inducing teleconnections (e.g., Koster et al. 2014; Wang et al. 2019), although internal atmospheric variability nevertheless remains a major factor (e.g., Hoerling et al. 2014; Park Williams et al. 2017).

Our analysis here is primarily focused on the impact of remote forcing from the tropics, including sea surface temperature (SST) anomalies, on the 2019 drought. This focus is partly motivated by the fact that the drought occurred contemporaneously with near-record positive values of the Indian Ocean dipole (IOD) (Doi et al. 2020). We assess the potential tropical impacts with regional replay experiments using the NASA GEOS-5 atmospheric general circulation model (AGCM; Molod et al. 2015); these are experiments in which the model simulations are constrained to remain close to an atmospheric

[1] https://www.ncdc.noaa.gov/sotc/drought/201909#national-overview.
[2] https://droughtmonitor.unl.edu/Maps/CompareTwoWeeks.aspx.

Corresponding author: Siegfried Schubert, siegfried.d.schubert@nasa.gov

DOI: 10.1175/JCLI-D-20-0428.1

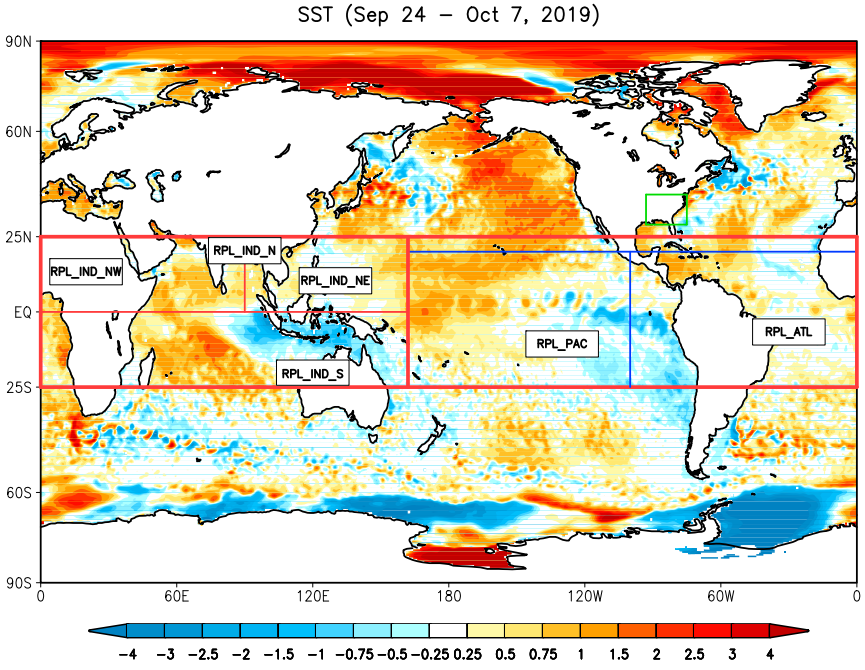

FIG. 1. Observed SST (°C) anomalies averaged over the period during which the southeastern United States (SEUS) experienced the largest precipitation deficits (24 Sep–7 Oct 2019. The green box outlines the SEUS region (29°–39°N, 93°–75°W) used to define the spatial averages shown in Fig. 8. The red boxes outline the various replay regions discussed in the main text (see Table 1). The blue lines define the subregions of the auxiliary replay runs discussed in the appendix (see Table A1).

reanalysis at each time step over selected regions external to the drought location (Schubert et al. 2019b; see next section). The experimental design allows us to identify the remote regions responsible for forcing the relevant circulation anomalies.

Section 2 describes the observational datasets and model simulations used in this study. Results are presented in section 3. Section 4 summarizes the results and addresses the question as to whether the drought was a freak (one-off) event that is unlikely to recur in the foreseeable future, or whether it is a sign of things to come. In the appendix we present the results of additional replay experiments that serve to aid in the interpretation of our main results, including an assessment of the sensitivity to the boundaries of the replay regions, the separate impacts of replaying in the tropical Pacific and Atlantic ocean basins, and the impact of the land surface conditions.

2. Data and model simulations

This study makes extensive use of the NASA Modern-Era Retrospective Analysis for Research and Applications, version 2 (MERRA-2; Gelaro et al. 2017). We note that the MERRA-2 precipitation used here as validation is an observationally corrected product (Reichle et al. 2011). We also make use of the SST fields provided by the Twentieth Century Reanalysis version 3 (Slivinski et al. 2019).

The study utilizes a number of AGCM simulations using the NASA Goddard Earth Observing System Model, version 5 (GEOS-5; Molod et al. 2015). The AGCM is essentially the same as that used to produce MERRA-2 but differs in two important ways. First, it is run here at a coarser (approximately 1°, compared to 1/2° for MERRA-2) horizontal resolution. Second, it includes a tendency bias correction (TBC) that helps alleviate some of the model's long-term biases (Chang et al. 2019).[3] The runs include a set of four simulations in which the AGCM is forced with observed SST covering the time period 1980–2019. This set of simulations, hereafter referred to NORPL_CLIM, is used to define the model's climatology.

A number of additional sets of AGCM simulations (30 ensemble members each) are also forced by observed SST but include different degrees of "regional replay" (i.e., they differ in the areas over which they are constrained to remain close to MERRA-2 at each time step). As described in Schubert et al. (2019b), during replay the AGCM's prognostic equations are modified to include an extra term consisting of the difference between the analysis (in this case MERRA-2) and a short term (6-h) model forecast (the analysis increment), thereby forcing the model to remain close to the reanalysis at each time step—in effect, specifics of the weather simulated in the specified region are forced to be accurate.

Figure 1 outlines the regions over which we carry out the various replay experiments, including the main experiments

[3] As described in Chang et al. (2019), the TBCs consist of time-averaged (over several decades) 6-hourly analysis increments (first guess forecast minus analysis) obtained from MERRA-2 data which are added with opposite sign as additional forcing terms to the model equations.

TABLE 1. List of the replay experiments discussed in the main text. The AGCM is the same model used to produce MERRA-2; however, it includes a tendency bias correction (TBC) as described in Chang et al. (2019). All runs are forced with observed daily mean SST. In the case of the four NORPL_CLIM simulations used to compute the model climatology, one run was a continuous 40-yr (1980–2019) simulation starting from MERRA-2 initial conditions. For the other three (in order to speed up the time to create a 40-yr climatology), each consists of 40 separate runs (one for each year, 1980–2019) initialized from the first continuous NORPL_CLIM run on 30 Jan and run through 1 Dec of that same year. In those runs, the atmosphere and land are initialized from each of the respective years of the continuous 40-yr simulation. The perturbations to the initial conditions for each of the 30 ensemble members were produced by taking the differences between two MERRA-2 atmospheric states separated by 1 day (using the 15 days prior to 30 Nov 2018), scaling those differences by 1/8, and adding them to (or subtracting them from) the initial state. Further information about that approach to perturbing initial conditions can be found in Schubert et al. (2019a).

Name	Time period	Initial conditions	Replay region	Ensemble members
NORPL_CLIM	1980–2019	MERRA-2/NORPL_CLIM	None	4
NORPL	30 Nov 2018–31 Dec 2019	MERRA-2	None	30
RPL_TR	30 Nov 2018–31 Dec 2019	MERRA-2	Tropics (25°S–25°N)	30
RPL_IND	30 Nov 2018–31 Dec 2019	MERRA-2	Indian Ocean region (25°S–25°N, 0°–162°E)	30
RPL_IND_N	30 Nov 2018–31 Dec 2019	MERRA-2	Northern Indian Ocean region (0°–25°N, 0°–162°E)	30
RPL_IND_S	30 Nov 2018–31 Dec 2019	MERRA-2	Southern Indian Ocean region (0°–25°S, 0°–162°E)	30
RPL_IND_NW	30 Nov 2018–31 Dec 2019	MERRA-2	Northwestern Indian Ocean region (0°–25°N, 0°–90°E)	30
RPL_IND_NE	30 Nov 2018–31 Dec 2019	MERRA-2	Northeastern Indian Ocean region (0°–25°N, 90°–162°E)	30

(thick and thin red lines; see Table 1 for a complete list of the experiments), and the auxiliary experiments discussed in the appendix (thin blue lines; see Table A1 for details of those experiments). For example, in RPL_TR (''replay tropics''; Table 1), the model is constrained to remain close to MERRA-2 at each time step in the latitude band 25°S–25°N (outlined by the thick red lines in Fig. 1). In RPL_IND (''replay Indian Ocean''; Table 1), the constraint is over the same latitude range, but confined to the longitudes 0°–162°E (the box with thick red lines centered on the Indian Ocean), and similarly for the subsets of the IND replay region outlined with the thin red lines in Fig. 1. In the NORPL simulations the model is free running (forced only by the observed SST), having no designated area of replay. Figure 1 also shows the global distribution of the SST anomalies averaged over the period during which the SEUS (outlined by the green box in Fig. 1) experienced the most intense precipitation deficits (24 September–7 October; see Fig. 2). We discuss the SST anomalies and their possible role in the development of the drought in the next section.

In section 3e, we also make use of a stationary wave model (SWM; Ting and Yu 1998) to compute the optimal forcing pattern for generating the wave structures that developed during the fall of 2019. The SWM is the dry dynamical core of a full nonlinear time-dependent AGCM with rhomboidal wavenumber-30 truncation in the horizontal and 14 unevenly spaced σ levels in the vertical. The basic approach to computing the optimal forcing is described in Schubert et al. (2011). It consists of first building up a collection of responses (using the SWM) to idealized heating located every 10° longitude and 5° latitude throughout the globe. The idealized heating at each location has the following characteristics: a sine-squared functional form, with horizontal scales of 20° longitude × 10° latitude with a maximum of 3 K day^{-1} in the middle troposphere. We then take the spatial inner product between each of the SWM responses and our target observed anomalies (in this case the contoured anomalies in the green box in Fig. 11c) and plot that value at each of the corresponding forcing locations. As such, we identify the extent to which the heating at any one location produces a response that resembles (projects onto) the observed anomalies. We interpret the map of those inner products as the ''optimal'' forcing pattern for the observed wave.

3. Results

We begin in section 3a with an overview of the evolution of the 2019 SEUS drought as determined from MERRA-2 and the various AGCM simulations described in section 2. This includes an investigation of how the tropics may have acted to force circulation anomalies responsible for the drought. For clarity, we partition our analysis of the drought into what appear to be three rather distinct 2-week periods. Specifically, section 3b focuses on the beginning of the drought (the *inception*, the first two weeks of September), while section 3c focuses on both the period of the most intense dry and warm anomalies (termed the *flash*, the last week of September and first week of October), and the period covering the drought's demise (the *recovery*, the last half of October). In section 3d we examine the uncertainties of the simulated anomalies as measured by the ensemble spread. Finally, in section 3e we look in more detail at the nature of the forcing of the Rossby waves, including an assessment of the role of the IOD.

We note that in all the results presented here, the MERRA-2 anomalies are computed with respect to the daily 1980–2019

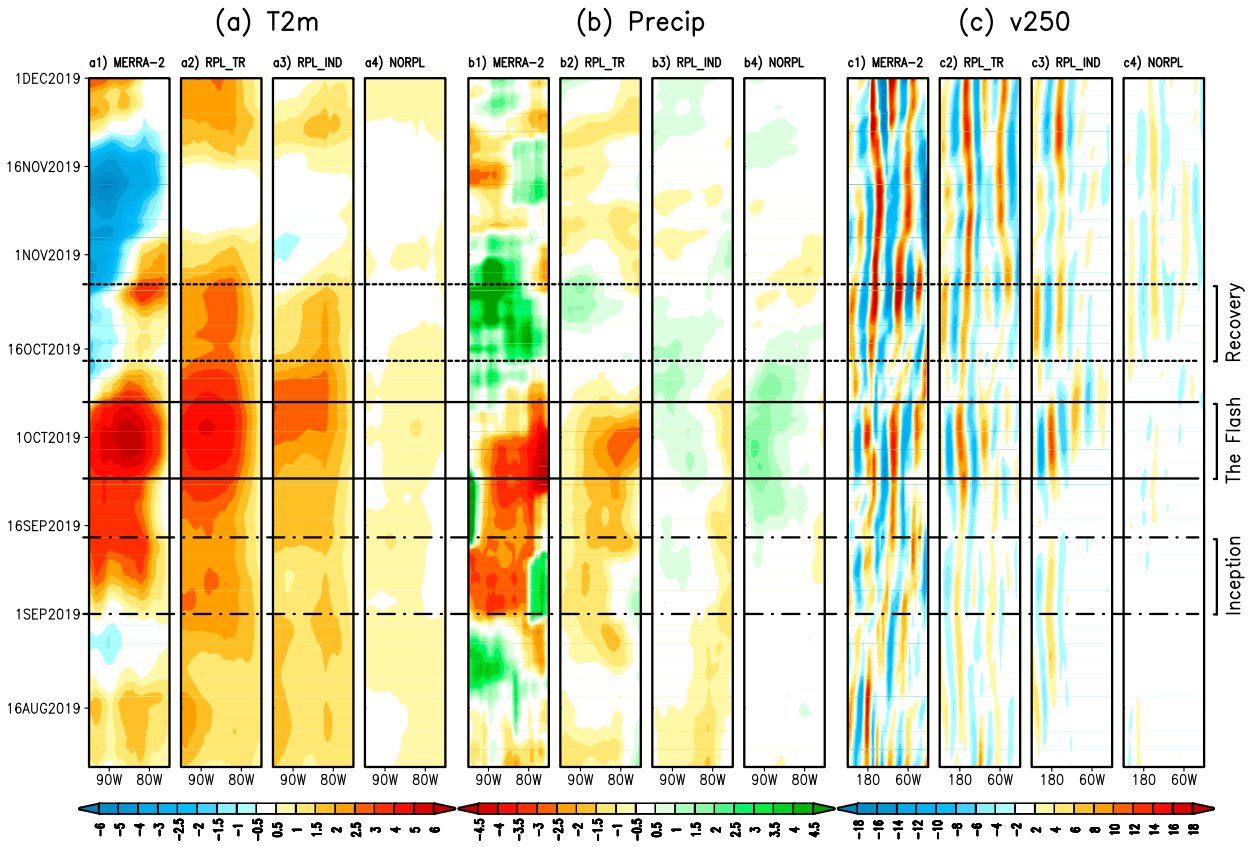

FIG. 2. Longitude–time plots of (a) 2-m temperature (T2m; °C; 95°–75°W), (b) precipitation (mm day^{-1}; 95°–75°W), and (c) 250-mb meridional wind (v250; m s^{-1}; 120°E–0°) anomalies for the period 1 Aug–30 Nov 2019. The T2m and precipitation anomalies are averaged between latitudes 29° and 39°N, while for the 250-mb v wind the average is between 30° and 55°N. All fields also have an 11-day running mean applied. For each set of panels, results are shown for MERRA-2, and the averages of 30-member ensembles of three different model simulations consisting of RPL_TR, RPL_IND, and NORPL (see Table 1). The heavy horizontal lines encompass the inception (1–14 Sep), flash (24 Sep–7 Oct), and recovery (14–27 Oct) periods.

MERRA-2 climatology. For the various AGCM simulations, the anomalies are computed relative to the daily climatology of the aforementioned NORPL_CLIM runs for the same period (1980–2019). Also, all the AGCM results presented here (with the exception of those shown in section 3d) represent averages over 30 ensemble members.

a. Evolution of the drought and links to the tropics

Figure 2 provides an overview of the evolution of the anomalous surface meteorology [2-m air temperature (T2m) and precipitation] over the drought region (see Fig. 1), along with a broader view of a key indicator of upper-tropospheric extratropical wave activity (the v-wind, averaged between 30° and 55°N) during late summer and fall of 2019. For each quantity the plots are organized (from left to right) to show results according to the strength of the constraints imposed on the AGCM by the observations, with the most strongly constrained (MERRA-2) on the far left, followed by RPL_TR, RPL_IND, and NORPL (the least constrained) on the far right. As such, by systematically relaxing the constraints on the model, the idea is that the runs should provide clues as to what factors (regions of the globe) are ultimately driving the temperature and precipitation anomalies over the SEUS.

It is clear from Fig. 2 [focusing on MERRA-2; see Figs. 2a(1), 2b(1), and 2c(1)], that the most intense T2m and precipitation anomalies develop quite rapidly during the flash period (24 September–7 October) concomitant with the development of an extratropical upper-tropospheric wave train spanning the North Pacific and North America. It is, however, also evident that the warm and dry anomalies begin to develop well before that, in early September (the inception). The only exception to the drying is the wet anomaly that occurs along the East Coast during the first week of September, a reflection (as noted above) of the impacts of Hurricane Dorian [Fig. 2b(1)]. Furthermore, the demise of the drought during the second half of October [the wet anomalies during the recovery period; Fig. 2b(1)] appears to be associated with the development of a second extratropical upper-tropospheric wave train [Fig. 2c(1)].

The simulations (Fig. 2) reproduce the various observed (based on MERRA-2) features to varying degrees, with RPL_TR [Figs. 2a(2), 2b(2), and 2c(2)] reproducing them most faithfully and the free-running AGCM (NORPL) showing little

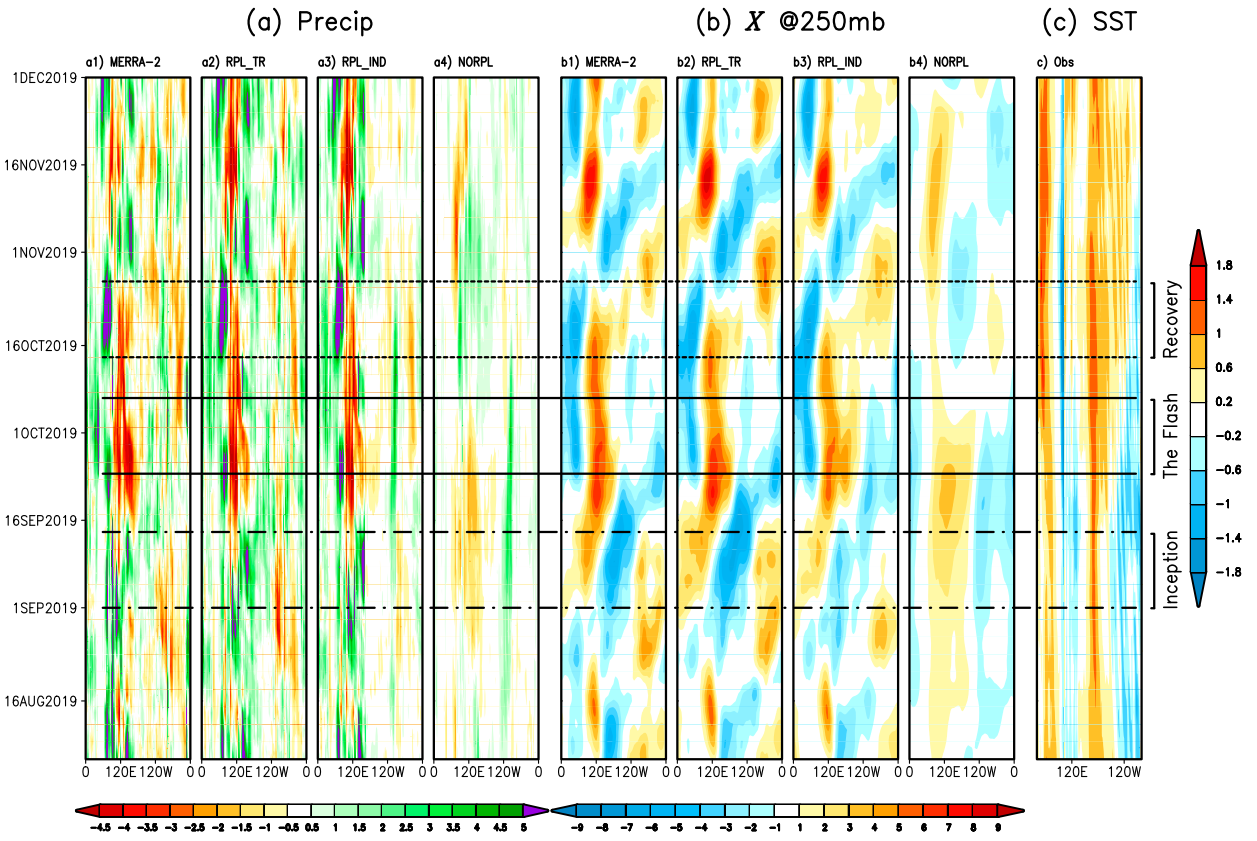

FIG. 3. Longitude–time plots of (a) precipitation (mm day^{-1}; averaged between the equator and 25°N), (b) 250-mb velocity potential (χ; 10^6 m^2 s^{-1}; averaged between 25°S and 25°N), and (c) the observed SST (°C; averaged between 5°S and 5°N, and displayed between 40°E and 80°W) anomalies for the period 1 Aug–30 Nov 2019. All fields also have an 11-day running mean applied. For the precipitation and velocity potential, results are shown for MERRA-2, and the averages of 30-member ensembles of three different model simulations consisting of RPL_TR, RPL_IND, and NORPL (see Table 1). The heavy horizontal lines encompass the inception (1–14 Sep), flash (24 Sep–7 Oct), and recovery (14–27 Oct) periods.

skill aside from the simulation of weak warm anomalies (Fig. 2a(4)]. In fact, NORPL shows a weak wet anomaly during the peak of the drought [Fig. 2b(4)], with little evidence of any wave activity during the peak of the event [Fig. 2c(4)]. Overall the model anomalies tend to be somewhat muted compared to those from MERRA-2, which is not unexpected given that they represent an average of 30 runs each. Comparing RPL_TR with RPL_IND, we see that constraining the atmosphere only over the region encompassing the Indian Ocean produces a substantial component of the temperature signal [cf. Figs 2a(2) and 2a(3)] and upper-tropospheric wave activity seen over North America [cf. Figs. 2c(2) and 2c(3)]. The temperature signal in RPL_IND, however, is nevertheless somewhat weaker and delayed relative to that in RPL_TR, and RPL_IND does not capture the observed precipitation anomalies [Fig. 2b(3)].

As a companion to Fig. 2, Fig. 3 examines the evolution of tropical quantities, including the tropical precipitation north of the equator (0°–25°N; Fig. 3a), the 250-mb velocity potential (25°S–25°N; Fig. 3b), and the equatorial (5°S–5°N) SST anomalies (Fig. 3c). Focusing on MERRA-2 in Fig. 3, we see that the inception period is characterized by enhanced precipitation in much of the central and western tropical North Pacific (approximately 100°–180°E), with reduced precipitation to the east [Fig. 3a(1)]. This is reflected in the upper-tropospheric velocity potential by the development of negative anomalies (indicating upward motion) in the central Pacific with positive anomalies (downward motion) situated both to the west and east [Fig. 3b(1)]. The strongest SST anomalies during that time are characterized by a narrow region of positive anomalies just west of the date line with negative anomalies to the east and west (Fig. 3c). In contrast, during the flash period large negative precipitation anomalies are established over the Pacific warm pool and eastern Indian Ocean (approximately 80°–150°E) with positive anomalies to the west [Fig. 3a(1)]. The associated velocity potential anomalies [Fig. 3b(1)] are characterized by an east (positive)–west (negative) dipole pattern situated between about 0° and 140°E occurring in conjunction with an east (cold)–west (warm) dipole pattern in the SST anomalies and a broadening of central tropical Pacific positive SST anomalies to the east (Fig. 3c). This basic east–west dipole pattern (in the precipitation, velocity potential, and SST)

continues from the flash period into the recovery period but with the western lobe showing more intense precipitation anomalies.

Ostensibly by design, RPL_TR largely reproduces MERRA-2 (both the precipitation and the velocity potential anomalies in Fig. 3), although there are reasons why an exact match is not guaranteed: the MERRA-2 precipitation shown here is not that produced directly by the model during the assimilation, being corrected by observations as described in Reichle et al. (2011), and the replay methodology adjusts the prognostic fields (Schubert et al. 2019b) rather than the precipitation itself. RPL_IND reproduces MERRA-2 precipitation within the "replayed" longitudes between 0° and 162°E, with little agreement with MERRA-2 precipitation east of those longitudes [cf. Figs. 3a(1) and 3a(3)]. Interestingly, the velocity potential anomalies produced in RPL_IND show a remarkable similarity to MERRA-2 at all longitudes [cf. Figs. 3b(1) and 3b(3)]; presumably, those anomalies reflect a response to the largest scales of the precipitation anomalies. Overall, the NORPL anomalies are weak, although there is some indication that the model is responding to the SST anomalies to produce enhanced precipitation near 120°W and reduced precipitation centered near 120°E during September [Fig. 3a(4)], and the associated velocity potential anomalies shown in Fig. 3b(4) are broadly consistent with MERRA-2 [Fig. 3b(1)].

The above results hint at potential teleconnections between the tropics and extratropics (including the SEUS). This potential linkage is explored next.

b. *The inception: A Matsuno–Gill response*

It is clear from MERRA-2 that warm [Fig. 2a(1)] and dry [Fig. 2b(1)] conditions were already developing in the SEUS at the beginning of September 2019. The land conditions prior to September provided no forewarning of an impending drought; in fact, the 2019 summer (June–August) precipitation anomalies were near or above normal over much of the central and eastern United States.[4] It thus appears that the local land conditions at the beginning of September did not play a role, and that the subsequent drought conditions that developed were instead driven primarily by external factors.

Figure 4 provides a global perspective on some of the relevant anomalies averaged over the first two weeks of September for both MERRA-2 and RPL_TR. While there was some weak extratropical upper-tropospheric Rossby wave activity during that time [see Fig. 2c(1)], it did not extend over the SEUS (not shown). Instead, in both MERRA-2 and RPL_TR, the clearest signal during this time is in the lower-tropospheric eddy streamfunction anomalies (Figs. 4c,d) and the upper-tropospheric velocity potential anomalies (Figs. 4a,b), both of which are consistent with a Matsuno–Gill-type tropical response (Matsuno 1966; Gill 1980) to the anomalous equatorial Pacific precipitation. The Matsuno–Gill-type response to equatorial heating can be interpreted as steady, damped Kelvin waves extending to the east and Rossby waves extending to the west of the region of heating (e.g., Showman and Polvani 2010). The anomalies consist of a quadrupole streamfunction anomaly pattern (Figs. 4c,d) straddling the equator over the tropical Pacific consisting of, at low levels, a pair of cyclonic anomalies to the west and anticyclonic anomalies to the east, with the latter producing anomalous anticyclonic flow that encompasses much of the southern United States. Furthermore, the associated anomalous Walker circulation (as reflected in the velocity potential anomalies; Figs. 4a,b) produces a tendency for descending motion over a broad region encompassing much of central America, the Intra-Americas Sea, and the SEUS.

We note that the similarity in Fig. 4 between MERRA-2 and RPL_TR is largely expected, since much of the domain of the Matsuno–Gill response lies within the replayed region (25°S–25°N). Nevertheless, again, the replay approach does not ensure that the observationally corrected MERRA-2 precipitation is reproduced exactly (cf. Figs. 4a,b). Also, differences in the AGCMs used to produce MERRA-2 and RPL_TR (section 2) likely contribute to small differences in the velocity potential and streamfunction anomalies. A similar Matsuno–Gill response occurs in RPL_IND but not in NORPL (not shown). In NORPL, the Matsuno–Gill response is both weaker and out of phase with that in the other runs. Apparently, NORPL does not capture the correct response to the imposed positive central/western tropical Pacific SST anomalies, producing precipitation anomalies that are in fact incorrectly negative in that region. The reasons for this are unclear; they presumably stem from model deficiencies, insufficient resolution, and fundamental issues with how a model responds to SST anomalies in that region when running uncoupled. We will return to this issue in section 4.

Returning to the time evolution of events, Fig. 3a(1) shows that the period of enhanced central and western equatorial Pacific precipitation [and the associated negative velocity potential anomalies; Fig. 3b(1)] develop rather abruptly at the beginning of September and then die out after a few weeks. These anomalies appear to be driven by the anomalous warm SSTs that developed just west of the date line at that time (Fig. 3c)—a time just after the tropical Pacific emerged from a weak El Niño event.[5] A noteworthy characteristic of the tropical Pacific SST anomalies during the inception period is the longitudinal confinement of the warm anomalies, an apparent result of the westward extension and strengthening of the cold tongue in the eastern tropical Pacific (Fig. 3c) together with the cold anomalies that developed to the west as part of the developing positive IOD. These two factors, we believe, acted to concentrate the region of the positive equatorial SST between about 160° and 180°E, thereby facilitating (as a result of the enhanced zonal SST gradients) a strong atmospheric response to the forcing in that region (Lindzen and Nigam 1987).

Figure 4e provides a map view of the SST anomalies during the inception period, showing the longitudinally confined nature of the warm tropical Pacific anomalies just west of the date line discussed above. It also shows the beginnings of the developing positive IOD (warm SST anomalies in the

[4] https://www.ncdc.noaa.gov/temp-and-precip/us-maps/3/201908#us-maps-select.

[5] https://www.climate.gov/news-features/blogs/enso/august-2019-el-ni%C3%B1o-update-stick-fork-it.

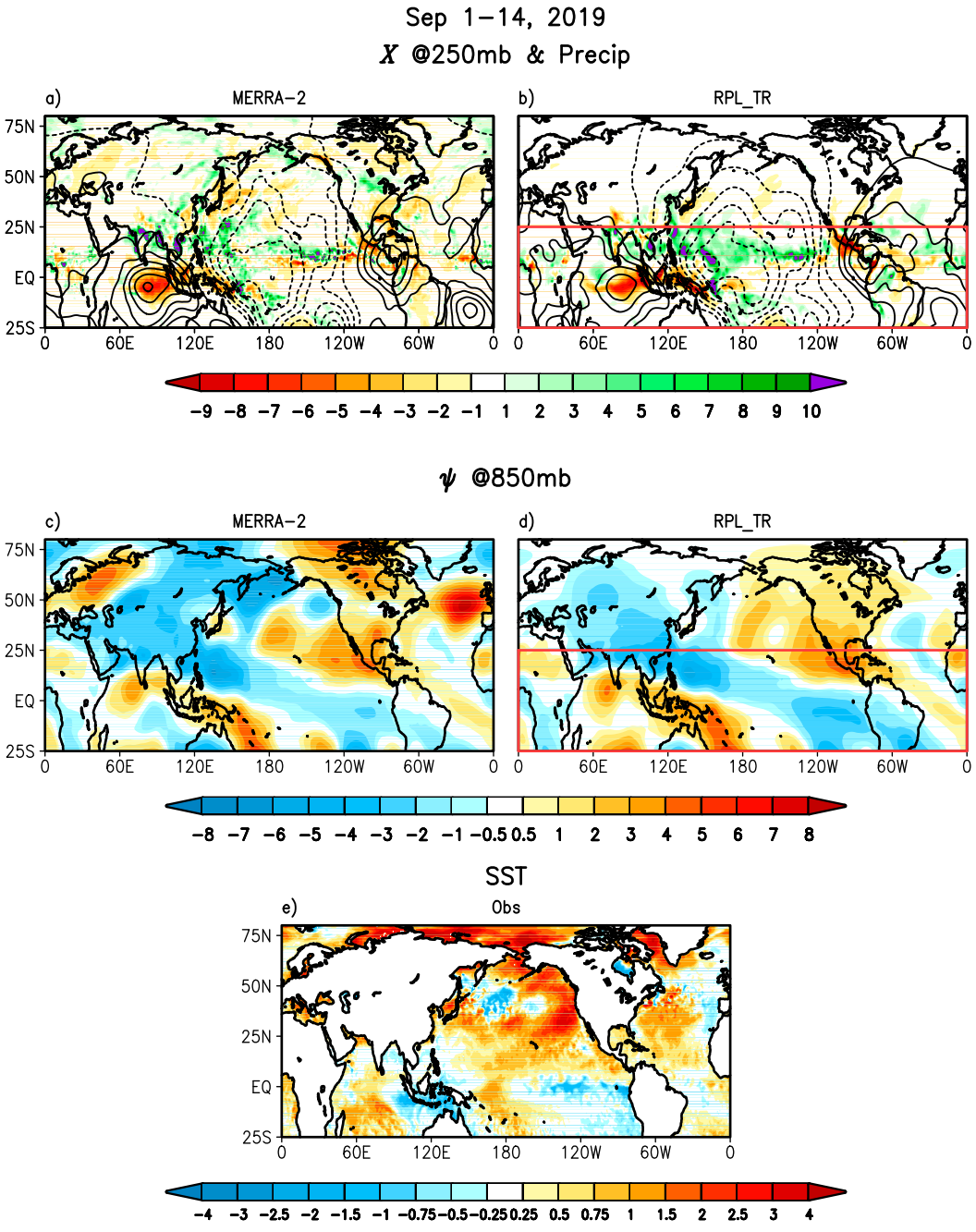

FIG. 4. (a),(b) The 250-mb velocity potential (χ; $10^6\,m^2\,s^{-1}$; contoured) and precipitation anomalies (shaded; mm day^{-1}) for MERRA-2 and RPL_TR, respectively. (c),(d) The 850-mb eddy streamfunction anomalies (Ψ; $10^6\,m^2\,s^{-1}$) for MERRA-2 and RPL_TR, respectively. (e) The observed SST anomalies (°C). All results are averaged over the *inception* period 1–14 Sep 2019.

western Indian Ocean and cold anomalies to the east), and very warm anomalies in the eastern North Pacific that appear to be the remnants of the very warm SST anomalies that developed earlier in the year. The latter had devastating marine impacts during that summer and appears to be the result of a weakened North Pacific high pressure system that was forced by central tropical Pacific and subtropical North Pacific SST anomalies (Amaya et al. 2020). The extent to which the North Pacific SST anomalies might have impacted the SEUS during early September is unclear, although there appears to be little signature of those anomalies in the North Pacific precipitation anomalies (Fig. 4a), suggesting that any feedback to the atmosphere from those SST anomalies is weak.

To summarize, it appears that the SEUS drought had its beginnings in the relatively narrow longitudinal band of positive SST anomalies that developed on the equator just west of the date line, anomalies that forced anticyclonic flow and a tendency for descending motion over the SEUS. These circulation changes acted to suppress convection over that region (with clear skies and sinking motion also leading to warming) and likely affected the development and tracking of tropical storms there (discussed further in section 4).

c. *The flash and recovery periods: The role of remotely forced Rossby waves*

The flash period (24 September–7 October) is characterized by the most intense T2m and precipitation anomalies over the SEUS. Focusing first on SST, we see that compared with the inception period, the warm central tropical Pacific SST anomalies during this time (Fig. 1) are no longer longitudinally confined (see also Figs. 3c and 4e) as the very active tropical instability waves have acted to erode the cold tongue to the east (e.g., Menkes et al. 2006). Also, the IOD has strengthened as a result of the development of warmer SST anomalies in the central and western Indian Ocean. It is also noteworthy that the North Pacific SST anomalies, especially those just off the west coast of North America, have weakened considerably.

Turning next to the atmosphere, we see from Fig. 5 (left panels) that during the flash period, in contrast with the inception period, well-developed Rossby wave trains (as reflected in the 250-mb eddy height anomalies) are quite evident in MERRA-2 (Fig. 5a), RPL_TR (Fig. 5b), and RPL_IND (Fig. 5c). The phasing of the waves, which span the North Pacific and North America, places a ridge over the eastern United States—likely a key factor in the rapid intensification of the drought conditions during this time (see below). Comparing RPL_TR and RPL_IND, it appears that the precipitation over the SEUS is sensitive to the exact placement and structure of the ridge, with the somewhat wider and weaker ridge structure of RPL_IND erroneously placing the main precipitation deficits off the coast (something we will come back to later).

Importantly, the results make clear that the wave is being forced from within the IND region. In that regard, MERRA-2, RPL_TR, and RPL_IND all show a dipole precipitation anomaly north of the equator in the IND region (dry over Southeast Asia and the Pacific warm pool region, with wet conditions to the west; Figs. 5a–c). These anomalies are reminiscent of those associated with the IOD, which achieved near-record positive values during this time [see section 3e(2)]. Also, as during the inception period, the NORPL run fails to produce the key tropical precipitation anomalies (in this case over the IND region, Fig. 5d), despite being forced with the observed SST.

We next turn to the recovery period (14–27 October), when substantial positive precipitation anomalies developed over the SEUS [Fig. 2b(1)], ending the drought. The 250-mb eddy height anomalies (right panels of Fig. 5) show again (as during the flash period) a clear signature of a Rossby wave train spanning the North Pacific and North America in MERRA-2 and in the various model runs (this time including NORPL; Fig. 5h). Focusing on the MERRA-2 results (Fig. 5e), the key difference with respect to the wave train from the flash period (Fig. 5a) is that the anomalous ridge over the eastern United States during the recovery period is situated farther east (centered on the East Coast, a roughly 90° phase shift). This, together with the anomalous trough to the west, facilitated poleward moisture flux (see below) and enhanced rainfall over much of the SEUS. Comparing the MERRA-2 (Fig. 5e) results with those of RPL_TR (Fig. 5f) and RPL_IND (Fig. 5g), it again appears that the impact on the precipitation over the SEUS is sensitive to the exact placement and structure of the ridge, with the model runs positioning the ridge somewhat northwest of the observed ridge, leading to weaker positive rainfall anomalies over the SEUS.

It appears from the above that the Rossby wave train that developed during the recovery is again forced from within the IND region. The precipitation anomalies in the IND region during the recovery period (Fig. 5e) differ from those during the flash period (Fig. 5a) in the development of stronger positive anomalies just west of the Indian subcontinent and weaker negative anomalies across Southeast Asia and the Pacific warm pool [see also Fig. 3a(1)]. The SST anomalies are overall similar to those of the flash period, with the main tropical differences being a somewhat stronger IOD, and a further erosion of the cold anomalies in the eastern tropical Pacific (see Fig. 3c). Exactly how these differences in the SST and precipitation anomalies lead, on a global scale, to what are rather subtle (but important, in terms of SEUS temperature and precipitation) shifts in the phase of the Rossby wave is not clear. (See the next section for further discussion.) As in the flash period, the AGCM during the recovery period (in the absence of replay) appears unable to produce the correct local precipitation responses to the SST anomalies in the IND region (cf. Figs. 5e,h). This likely contributes to a weaker wave train for NORPL, one that does not extend southeastward to North America.

Figure 6 provides a more detailed look at the precipitation anomalies over the SEUS (with 850-mb moisture flux anomalies superimposed) during the flash and recovery periods. The observed (MERRA-2) dry precipitation anomalies in the SEUS during the flash period (Fig. 6a) are accompanied by wet anomalies to the north and west. This juxtaposition of the dry and wet anomalies reflects what appears to be a barotropic structure of the upper-level ridge, which results in anticyclonic flow of low-level moisture below the ridge. This is characterized by northeasterly flow off the coast and southwesterly flow over the central United States. As such, while the wet anomalies in the central United States are likely the result of the enhanced southerly flux of moisture into that region, the dry anomalies in the SEUS (which are centered on the low-level anticyclonic circulation anomaly) more likely result from the tendency for descending motion to occur in the center of the anomalous ridge. RPL_TR (Fig. 6b) reproduces much of the anomalous moisture flux over the continent, but not the northeasterly flux off the coast; this reflects the overall eastward shift of the upper-level anticyclonic anomaly, which keeps the most intense dry anomalies over Florida and off the East Coast. Both RPL_IND (Fig. 6c) and NORPL (Fig. 6d) fail to produce the dry anomalies in the SEUS. For RPL_IND, this

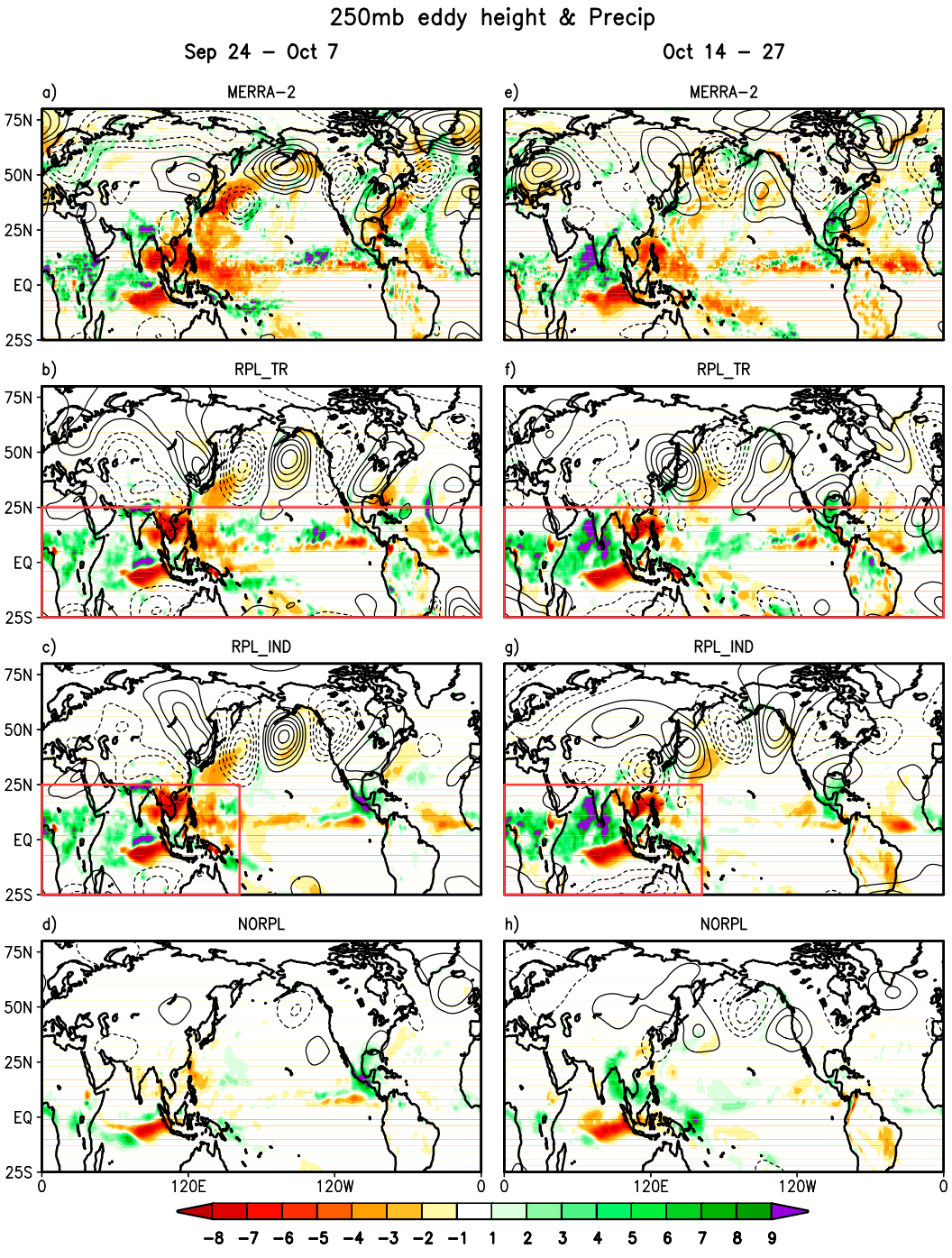

FIG. 5. (left) The 250-mb eddy height (contoured) and precipitation anomalies (shaded; mm day^{-1}) for (a) MERRA-2, (b) RPL_TR, (c) RPL_IND, and (d) NORPL averaged for the period 24 Sep–7 Oct 2019 (height contours are every 40 m for MERRA-2 and 20 m for the model). (right) As in the left column, but for the period 14–27 Oct 2019.

appears to be due to deficiencies in the structure and placement of the ridge over the United States, although RPL_IND does reproduce the observed enhanced southerly moisture flux into the central United States.

During the recovery, the observed (MERRA-2) enhanced precipitation anomalies (Fig. 6e) in the SEUS are associated with enhanced southerly moisture flux into that region, reflecting a southeastward shift in the upper-level positive height anomaly

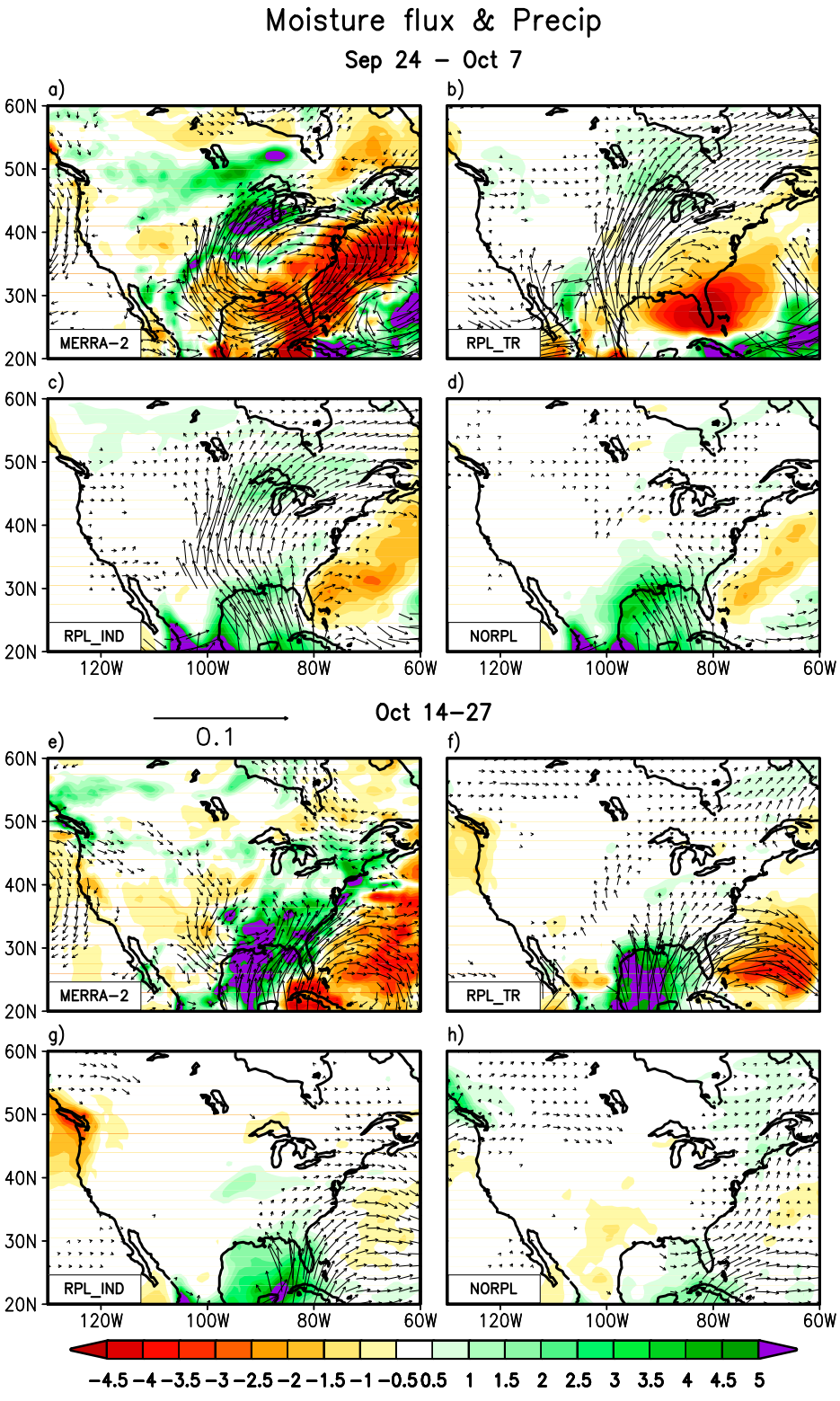

FIG. 6. The precipitation (shaded; mm day^{-1}) and 850-mb moisture flux anomalies (vectors; kg m s^{-1}) averaged over the period 24 Sep–7 Oct 2019 shown for (a) MERRA-2, and the model runs (b) RPL_TR, (c) RPL_IND, and (d) NORPL. (e)–(h) As in (a)–(d), but for the period 14–27 Oct 2019. For clarity, the MERRA-2 moisture fluxes (which represent a single realization compared with an average of 30 for the model) are divided by 2.

(Fig. 5e). This is reproduced to some extent in RPL_TR (Fig. 6f) and RPL_IND (Fig. 6g), although these experiments place the most intense positive precipitation anomalies farther south, over the Gulf of Mexico. In contrast, the anomalies (precipitation and moisture flux) in NORPL (Fig. 6h) again bear little resemblance to the observed.

Shown in Fig. 7 are T2m anomalies during the flash and recovery periods with the corresponding 250-mb eddy height anomalies superimposed. During the flash period (Figs. 7a–d), only NORPL (Fig. 7d) fails to reproduce the overall warming that occurred over the eastern United States. The strong link between T2m and the upper-tropospheric height anomalies is clearly evident in MERRA-2 (Fig. 7a) with the Rossby wave discussed earlier producing a northwest trough–southeast ridge pattern in phase with the cold–warm T2m anomalies. This same connection is reproduced in RPL_TR (Fig. 7b) and RPL_IND (Fig. 7c) but is absent in NORPL (Fig. 7d), which, again, failed to reproduce the Rossby wave. We note that while the RPL_IND results show no evidence of the pronounced cold anomalies juxtaposed with the large negative height anomaly in the northwest (the MERRA-2 results in Fig. 7a), this appears to primarily reflect a statistical sampling issue (internal atmospheric variability), with a few of the individual ensemble members (not shown) indeed showing cold anomalies that are not dissimilar to those found in the MERRA-2 results.

The recovery period (Figs. 7e–h) also shows a clear link between T2m and upper-tropospheric height anomalies. In MERRA-2 (Fig. 7e), the anomalous ridge and trough pattern is positioned farther to the southeast compared to that in the flash period, and RPL_TR (Fig. 7f) and RPL_IND (Fig. 7g) again reproduce aspects of the observed (MERRA-2) anomalies. NORPL (Fig. 7h), on the other hand, produces warm anomalies in the western United States reflecting an anomalous upper-level ridge on the West Coast linked to the North Pacific Rossby wave produced in those runs (Fig. 5h).

The above results highlight the sensitivity of the T2m and especially the precipitation anomalies to the exact location (phase), structure, and amplitude of the Rossby waves over North America. While RPL_TR reproduces the anomalies reasonably well, that is not the case for RPL_IND especially for the flash period, during which it places the precipitation deficits off the coast. Understanding why RPL_TR gets this about right while RPL_IND does not require a closer look at the sensitivity of the results to the boundaries of the replay region and the potential interactions with the circulation in the other (eastern Pacific and Atlantic) tropical ocean basins. The results, which suggest only minor impacts (independent of the Indian Ocean–forced wave train) from the other ocean basins, are discussed in the appendix where we examine the results of additional replay experiments.

We next look into the uncertainties of the model results as expressed by the spread of their 30 ensemble members.

d. Uncertainty: The ensemble spread

When comparing the model results with those from MERRA-2, it helps to think of the latter as a single realization (outcome) of a range of paths nature could have taken. As such, an important constraint in judging the verisimilitude of the model results is whether or not the observed outcome falls within the ensemble spread (uncertainty) of the model results. Note, however, that because the ensemble spreads of our model simulations are presumably suppressed artificially through the use of replay and because the SSTs are specified, these spreads must be interpreted with caution. Also, keep in mind that because all of the model runs were initialized long enough before the drought developed (see Table 1), the initial atmospheric and land conditions should have little impact.

The time evolution of the area-averaged (see green box in Fig. 1) SEUS T2m and precipitation anomalies is shown in Fig. 8 for each ensemble member. For T2m the RPL_TR (Fig. 8a) runs generally track the MERRA-2 values, although they do not capture the November cold anomalies; the ensemble mean remains above normal throughout the fall. T2M results for RPL_IND (Fig. 8b) are similar, although with somewhat weaker positive anomalies and somewhat larger ensemble spread (fully encompassing MERRA-2), especially during November. In contrast, the ensemble mean T2m for NORPL (Fig. 8c) shows generally weak positive anomalies throughout the period, with the spread growing monotonically throughout the fall and not capturing the MERRA-2 maximum during the flash period.

Results for precipitation (Figs. 8d–f) are similar to those for T2m, although with the models reproducing the most extreme anomalies with less success. In the RPL_TR runs (Fig. 8d), for example, the most extreme MERRA-2 positive values that developed during the recovery period in the second half of October lie at the very edge of the ensemble spread, suggesting that this is indeed a very rare event. It is of course possible that the RPL_TR runs are producing an overly optimistic assessment of the uncertainty (the ensemble spread is too small) given that we are constraining the tropics. Model error might also be contributing to insufficient spread, although addressing what might be causing that is beyond the scope of this study. Both RPL_IND (Fig. 8e) and NORPL (Fig. 8f) have insufficient spread to encompass the dry anomalies in September, with the NORPL run exhibiting an ensemble mean that is in fact both weak and out of phase with the observed anomalies.

To delve further into the uncertainties in the Rossby wave responses during the flash and recovery periods, we now focus on uncertainties in RPL_IND, for which the replay region encompasses the underlying Rossby wave forcing and yet is far enough removed from the drought itself to provide some insight into the robustness of the Rossby wave structure in the drought region. Figures 9a and 9b show the signal-to-noise ratio (S/N) of the 250-mb eddy height anomalies for the flash and recovery periods, respectively. The flash period (Fig. 9a) shows a very robust Rossby wave signal with S/N values exceeding 4 over the North Pacific and exceeding 2 over much of the southern United and northern Mexico. It is noteworthy that S/N is relatively weak over the West Coast (with values $<$ 1.5), presumably reflecting greater variability in the position and strength of the anomalous trough, which is located at the inflection point between the exit region of the North Pacific jet and entrance region of the North American–North Atlantic jet. The recovery period similarly shows a robust Rossby wave signal (Fig. 9b) across the North Pacific, with S/N again being

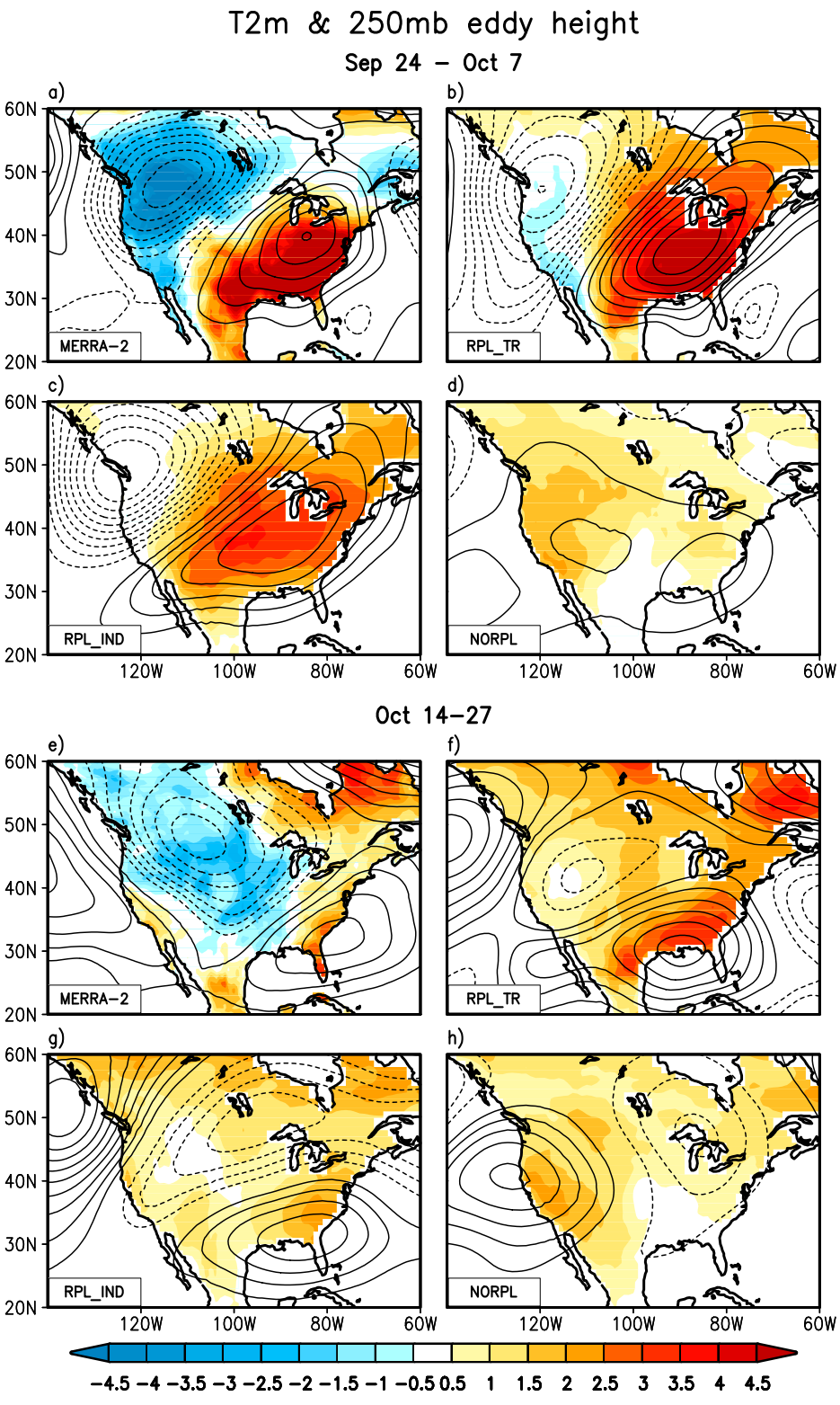

FIG. 7. T2m (°C, shaded) and 250-mb eddy height anomalies (contoured) for (a) MERRA-2, and the models runs (b) RPL_TR, (c) RPL_IND, and (d) NORPL averaged over the period 24 Sep–7 Oct 2019. (e)–(h) As in (a)–(d), but for the period 14–27 Oct 2019. For clarity, the height contour intervals are 40 m for MERRA-2 and 20 m for the model results (which are an average of 30 ensemble members).

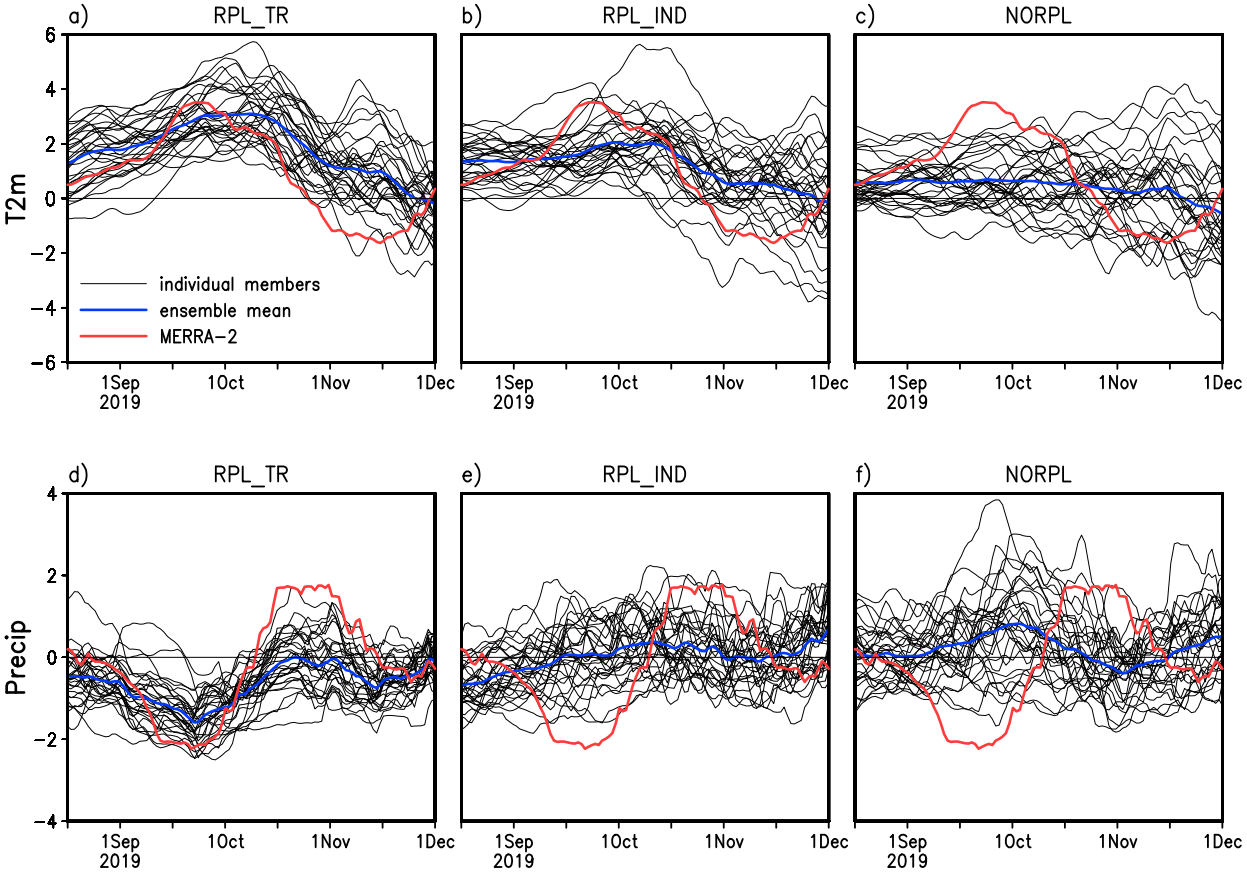

FIG. 8. Time evolution of the 30 individual ensemble members averaged over the SEUS (93°W–75°W, 29°–39°N; see Fig. 1) with a 31-day smoother applied, for (top) T2m (°C) and (bottom) precipitation (mm day^{-1}) for the model runs (a),(d) RPL_TR, (b),(e) RPL_IND, and (c),(f) NORPL. In each case, the blue lines are the ensemble mean, and the red lines are from MERRA-2.

relatively large over southeastern North America, where the anomalous ridge extends southward over the Gulf of Mexico.

While the above results show that the waves that occurred during the flash and recovery clearly have substantial S/N values in the extratropics, it is not yet clear that the two waves are fundamentally different in character—in particular, that the apparent differences in their phases rise above the noise of internal atmospheric variability. This is addressed in Fig. 9c, which shows that the difference between the waves during the recovery and flash periods (which itself has a clear wave structure, reflecting a phase shift) are indeed highly significant. We are thus confident in saying that the difference between the two waves reflect actual differences in their physical drivers during these two periods. This leads us to look now in more detail at the Rossby wave forcing in the Indian Ocean (IND) region.

e. On the nature of the Rossby wave forcing

There are a number of unanswered questions regarding the nature of the Rossby waves that occurred during the flash and the recovery periods. While it seems clear that the forcing of the waves occurred within the IND region, it is less clear exactly which aspects of the forcing anomalies (precipitation and associated heating) were most important and whether the relevant precipitation anomalies are strongly tied to SST anomalies. The fact that NORPL fails to produce the Rossby waves would suggest little impact from the SST anomalies, although as noted above that could be due to model deficiencies or to the lack of ocean–atmosphere coupling in our simulations. Finally, there is the question of how unique these Rossby waves are. Have similar events occurred in the past, and should we expect more to occur in the future? The answer to that requires a better understanding of the nature of the wave forcing.

As a first step, in order to better isolate those regions within the IND region that are the primary drivers of the Rossby waves, we have carried out additional experiments replaying to subregions of the IND region consisting of 1) the southern IND region, 2) the northern IND region, 3) the northwestern IND region, and 4) the northeastern IND region (see Table 1 and Fig. 1 for an outline of the regions). The results are shown in Fig. 10 for the 250-mb v-wind anomalies where, for convenience, we have included the results for MERRA-2 and the full IND region (already shown in Fig. 2c). Comparing Fig. 10b (RPL_IND), Fig. 10c (RPL_IND_N), and Fig. 10d (RPL_IND_S) it is clear that the source of the Rossby wave lies north of the equator. In fact, comparing Fig. 10e (RPL_IND_NW) and Fig. 10f (RPL_IND_NE) we see that it is for the most part the

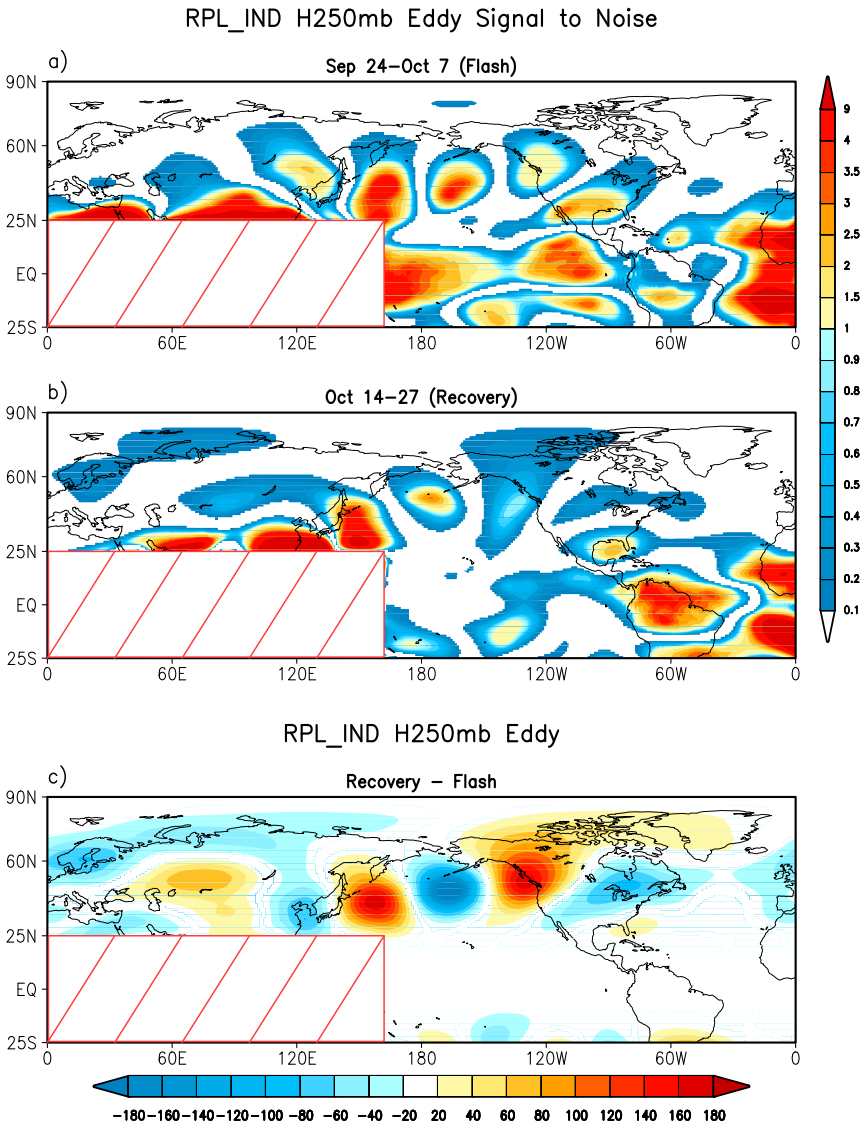

FIG. 9. The signal-to-noise ratio (S/N) of the 250-mb eddy height anomalies averaged for the (a) flash and (b) recovery periods for the RPL _IND runs. Here S/N is defined as the ratio of the squared ensemble mean anomaly divided by the intraensemble variance. The IND region is masked out (with hashing), since the S/N is undefined (there is no noise) in the replayed region. (c) The differences between the ensemble mean 250-mb eddy height (m) during the recovery and flash periods (recovery minus flash). Values in (c) are masked out that do not achieve a statistical significance level of at least 5%, based on local *t* tests.

northeast quadrant of the IND region that is forcing the Rossby waves during both the flash and recovery periods. While there does appear to be some weak impact on the 250-mb v-wind from the northwest quadrant of the IND region RPL_IND_NW (Fig. 10e) during the recovery, the impact is strongest during the second half of November, well after the time period of interest here.

1) AN OPTIMAL FORCING APPROACH

To further isolate which aspects of the forcing matter most for generating the Rossby wave responses, we could continue to decrease the size of the regions being replayed. This, however, has obvious computational drawbacks and (based on our experience with regional replay) can produce results that are difficult to interpret. For technical reasons, the replayed region cannot be too small; the approach seems to work best when the region is large enough to allow the magnitudes of the increments to be similar to those of the analysis increments originally produced by MERRA-2. We thus take a different approach to isolating the forcing of the Rossby waves: the use of a SWM (see section 2).

Given the simplicity of the SWM and the idealized nature of the forcing that it utilizes, we focus here on monthly means. We

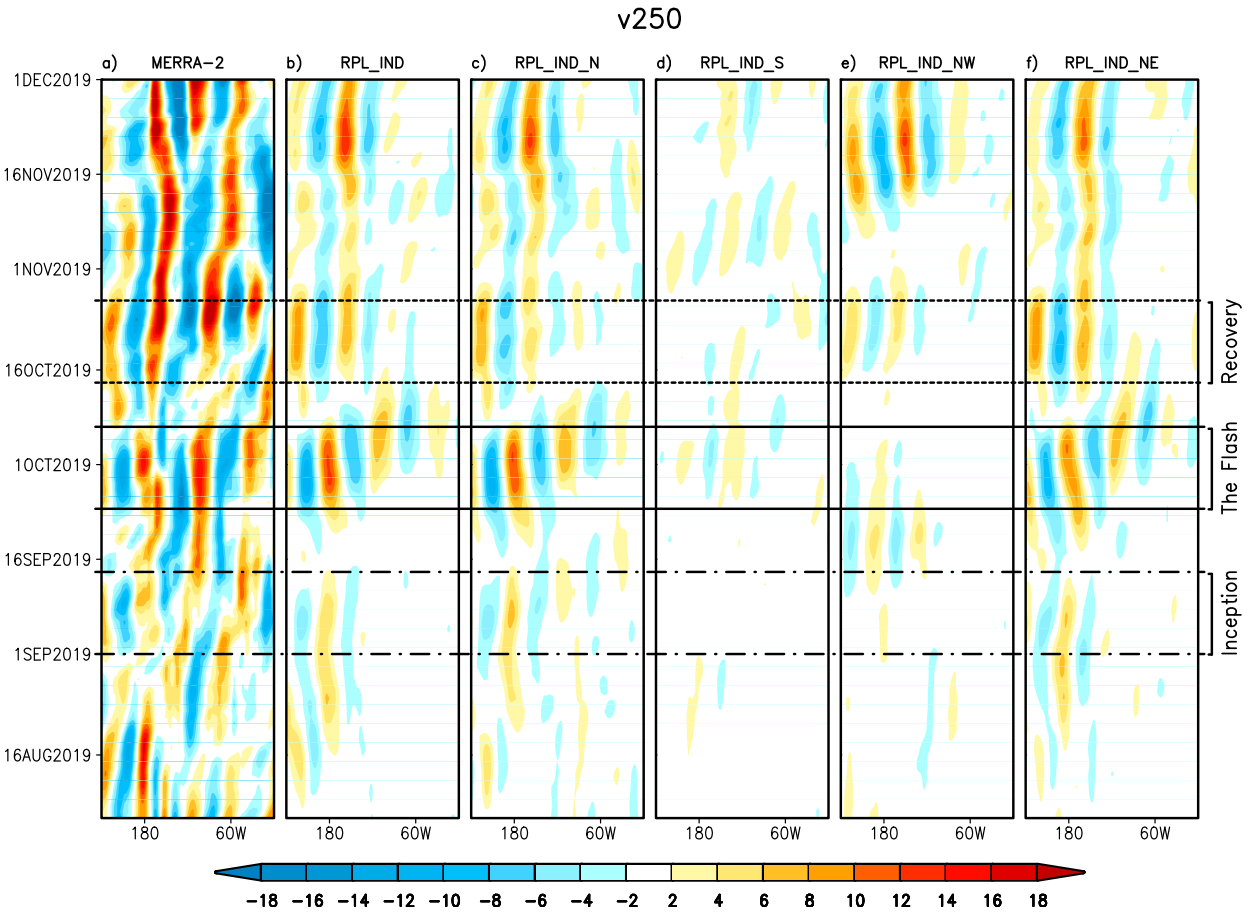

FIG. 10. Longitude–time plots of the 250-mb meridional wind (v250; m s^{-1}; 120°E–360°) anomalies for the period 1 Aug–30 Nov 2019. The fields are averaged between 30° and 55°N, and an 11-day running mean is applied. Results are shown for (a) MERRA-2, and the averages of 30-member ensembles for (b) RPL_IND, (c) RPL_IND_N, (d) RPL_IND_S, (e) RPL_IND_NW, and (f) RPL_IND_NE (see Fig. 1 and Table 1 for definitions of the regions). The heavy horizontal lines encompass the inception (1–14 Sep), flash (24 Sep–7 Oct), and recovery (14–27 Oct) periods.

focus in particular on October (instead of September) because it is the dynamically more active month (see Fig. 2c) and is likely most representative of the waves of interest here (those that developed during late September/early October and the second half of October of 2019). Our goal here is to use the SWM to identify those regions where a heat source/sink produces a response that resembles the observed October wave structure (shown as black contours within the green box in Fig. 11c). Recall (see section 2) that we do that by taking the inner products between the observed wave structure and all the SWM's responses to idealized heat sources located throughout the globe (spaced 10° longitude and 5° latitude apart). The optimal forcing pattern is just a map of those inner products plotted at the forcing locations. Figure 11a shows that the optimal forcing pattern for the observed October wave itself has a wavelike structure, which is to a large extent embedded within the climatological jet. Note that the optimal forcing pattern for the September anomalies is substantially weaker, presumably reflecting in part the weaker North Pacific jet during that month (not shown).

The optimal forcing pattern can also be thought of as a global sensitivity map quantifying the extent to which heating in a particular region can produce a response resembling the observed. As such, it does not say anything about which of the observed heating anomalies may have actually produced the observed response. That requires that we multiply the optimal forcing pattern (or sensitivity map) by an estimate of the actual October 2019 heating anomalies (Fig. 11b). The results of that product are shown in Fig. 11c. Here, we mask out the values in the target region (values within the green box) with the understanding that, while they may represent regions of potential feedbacks once the wave develops, they are unlikely to be the original source of the wave. The results suggest that the heating anomalies over Southeast Asia and India (and regions immediately to the northwest and south) are likely most responsible for the development of the October mean 2019 Rossby wave—a result that is consistent with our finding about the importance of the northeast quadrant of the IND region (Fig. 10f) . (Note that only positive values in Fig. 11c would produce the correct sign of the

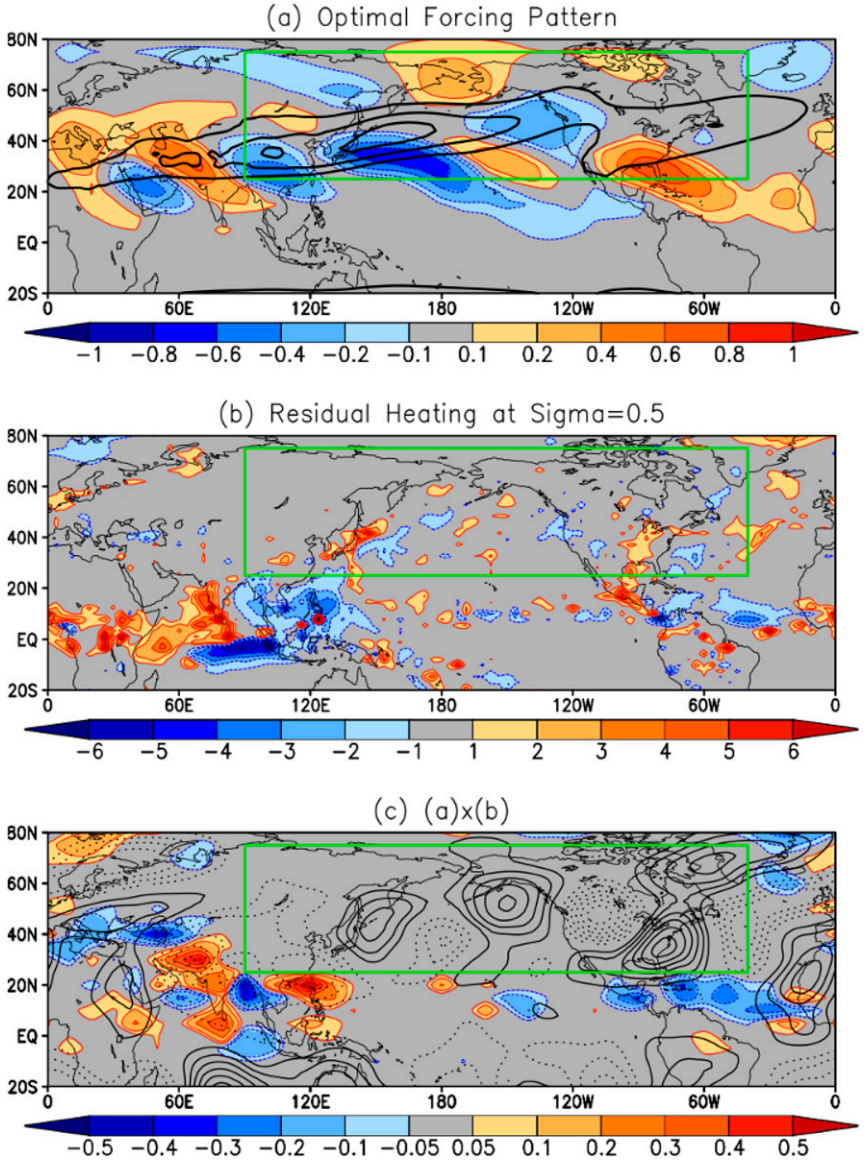

FIG. 11. (a) The optimal forcing pattern (shaded) for the observed (MERRA-2) October 2019 upper-tropospheric eddy streamfunction anomalies [contoured in (c)] in the region outlined by the green box. Results are based on the SWM's responses to idealized forcing functions distributed throughout the globe (see section 2 for details). The contours (20, 30, 40, and 50 m s^{-1}) are the climatological (1980–2019) October 250-mb zonal wind from MERRA-2. (b) The estimated observed October 2019 heating anomalies in the mid troposphere computed as a residual from MERRA-2 (°C day^{-1}). (c) The product of the heating anomalies and the optimal forcing pattern (shaded, with the values within the green box masked out). The contours are the observed (MERRA-2) October 2019 upper-tropospheric eddy streamfunction anomalies (interpolated to the SWM's sigma level = 0.257, contour interval is 2×10^6 m^2 s^{-1} with negative contours dashed).

wave.) Those regions are associated with the equatorward (south of the jet) extension of the lobes of the optimal forcing pattern over southern Asia. Note that the east–west alternating sign of the optimal forcing pattern in that region (Fig. 11a) allows the observed heating anomalies of late September and October of 2019 (presumably linked to the IOD; see the next section) to be especially effective in producing the wave response.

2) THE LINK TO THE IOD

The dipole structure of the heating anomalies in the IND region during September and October of 2019 appears to be

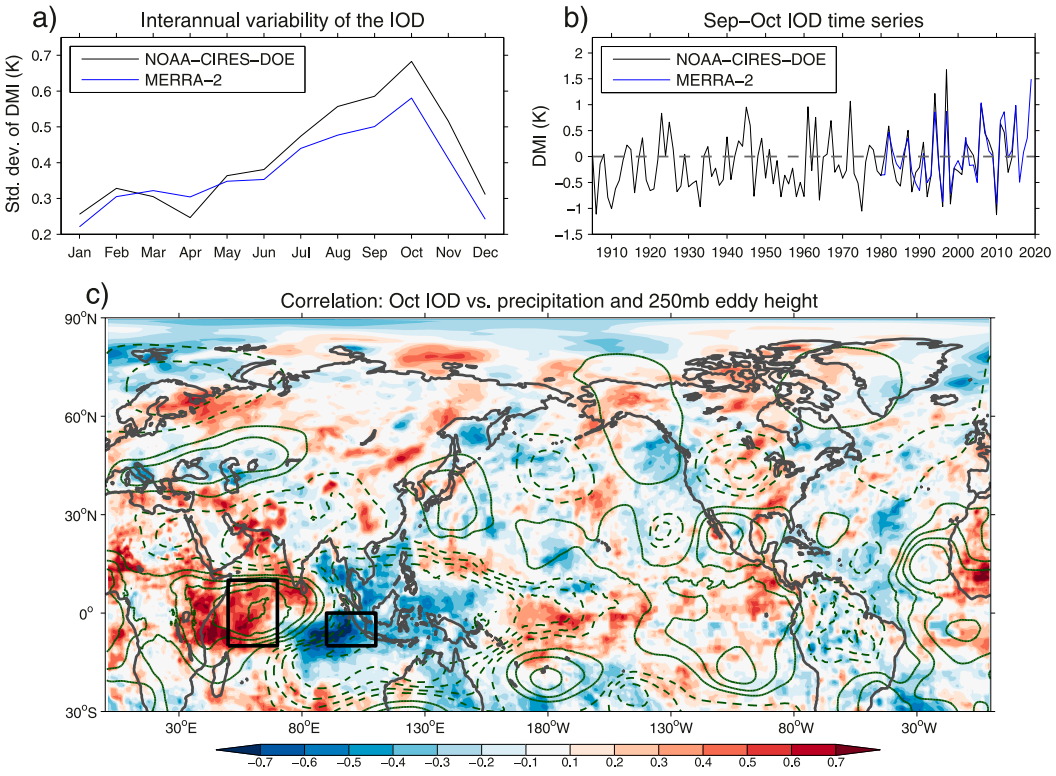

FIG. 12. (a) The interannual standard deviation of the IOD as a function of month in MERRA-2 and the NOAA-CIRES-DOE (version 3) Twentieth Century Reanalysis over the period 1980–2015. The Dipole Mode Index (DMI) is used to quantify the IOD and is defined as the difference in regional-mean SST anomalies between western (10°S–10°N, 50°–70°E) and southeastern (10°S–0°, 90°–110°E) tropical Indian Ocean regions [shown as black boxes in (c)]. (b) Time series of the September–October average IOD for both datasets (the reference climatology is 1980–2015). (c) Correlations between the October monthly mean IOD index and precipitation (shaded) and between the IOD index and 250-mb eddy height (green contours) based on MERRA-2 for the years 1980–2019. Moderate and strong ENSO years (in which the Oceanic Niño Index equals or exceeds a magnitude of 1.0, based on Climate Prediction Center data; see https://origin.cpc.ncep.noaa.gov/products/analysis_monitoring/ensostuff/ONI_v5.php) are not included (El Niño years: 1982, 1987, 1997, 2002, 2009, 2015; La Niña years: 1988, 1995, 1998, 1999, 2007, 2010, 2011). Contours for eddy height correlations are draw every 0.15 (omitting zero) with negative contours dashed.

consistent with the local precipitation response to the positive phase of the IOD (Saji et al. 1999; Webster et al. 1999). While such a dipole structure also suggests a possible role of the Madden–Julian oscillation (MJO), it turns out the MJO was not particularly active during most of September and October of 2019. There was some indication of the MJO being active and in phase 1 [based on the real-time multivariate MJO (RMM) index; Wheeler and Hendon 2004] during the second half of September, but there was little eastward propagation of the signal and a concern that the RMM was erroneously projecting onto the developing IOD.[6] In any event, phase 1 would suggest an MJO impact consisting of increased precipitation over the Southeast at least for the cold season (Arcodia et al. 2020), something that is clearly at odds with what actually occurred in September.

Here, we look more generally at the impact of the IOD SST anomalies, including their impact on Rossby wave development. We also attempt to put the 2019 event in the context of the longer climate record. The IOD is well known to be especially active during the boreal fall season. Figure 12a shows that, indeed, it is during the boreal fall months (especially September and October) that the IOD has the greatest interannual variability. An examination of the long-term (1905–2019) record of the September/October IOD (Fig. 12b) reveals a period of unusually strong activity starting in the early 1990s, with 2019 being an exceptionally strong positive event. While there appears to be some tendency for weaker activity during the earlier periods, the record is interspersed with periods of weak and strong activity. Accordingly, and also taking into account the reduced SST observational coverage during earlier periods, it is unclear whether recent decades are truly different (more active) than earlier

[6] https://www.cpc.ncep.noaa.gov/products/precip/CWlink/MJO/ARCHIVE/PDF/.

decades, although it does appear that the recent period is characterized by a higher number of positive events (e.g., Cai et al. 2009). Indeed, a number of studies support the idea that IOD activity, rather than being characterized by a secular trend, undergoes multidecadal fluctuations (e.g., Ihara et al. 2008).

With this in mind, we focus on the recent four decades (1980–2019) spanned by MERRA-2 data to compute the correlations between the October IOD and both precipitation and the 250-mb eddy height (Fig. 12c). Here we have removed moderate and strong ENSO years (see Fig. 12 caption) in order to minimize any impact from such events. To the extent that the IOD at times occurs concurrently with ENSO, we are likely missing some of the IOD impacts; nonetheless, the correlations with precipitation in the IND region show a clear dipole pattern consistent with the actual precipitation/heating anomalies that occurred in 2019 (cf. Fig. 11b). Furthermore, there is evidence of a wave structure from the correlations with the 250-mb eddy height that spans the North Pacific and North America, not unlike that of the actual eddy heights that developed during October 2019 (cf. Fig. 11c). It is also worth noting that, while there are weak negative correlations between the IOD and precipitation along the East Coast indicating a tendency for dry conditions there when the IOD is positive, the correlations just to the west (over the U.S. Gulf states) are stronger and positive (Fig. 11c), indicating a tendency for wet conditions over that region when the IOD is positive. This latter finding is consistent with a recent study, that of Strong et al. (2020), showing that Rossby waves emanating from the Indian Ocean are linked to a shift toward generally wetter conditions in the eastern United States in the early 1970s. That both wet or dry conditions in the eastern United States may originate from a positive IOD (as shown here) stresses the need to better understand the phasing of Rossby waves as they emanate from the IND region. Given our incomplete understanding of what determines Rossby wave phase, combined with the fact that the Indian Ocean has warmed considerably in recent years, it is unclear whether we should expect a historically robust link between the IOD and precipitation in the SEUS.

On that note, it remains to be seen exactly how the within-season (late September to late October) changes in the heating may have acted to produce the two slightly different Rossby waves during the flash and recovery periods during 2019. For example, was the change in forcing/heating part of a systematic seasonal (September to October) evolution of the local precipitation response to the IOD, or did it simply reflect unforced random fluctuations? Of course, it is also possible that the differences in the Rossby waves resulted primarily from differences in the prevailing North Pacific–North American waveguide during those two periods, which in turn could reflect either systematic seasonal changes or unforced variability of the midlatitude jets. In fact, the North Pacific jet undergoes substantial changes between late September and late October, both strengthening and shifting equatorward (not shown).

4. Discussion and conclusions

In summary, our regional replay experiments have allowed us to isolate the underlying causes of the fall 2019 SEUS drought. We found that the period with the most extreme dry and warm conditions (the *flash* period in late September and early October of 2019) and the subsequent *recovery* period in the second half of October were driven by two different Rossby wave trains emanating from the tropics in the region of the Indian Ocean. Furthermore, we have evidence that the forcing (heating) for both waves was tied to the development of near-record positive values of the IOD during that fall. This contrasts with the initial development of the drought during the first two weeks of September (the *inception* period), which was caused by anomalous low-level anticyclonic flow and a tendency for suppressed vertical motion over the southeastern United States (SEUS) and surrounding regions that appears to have suppressed the occurrence of landfalling hurricanes. In fact, as reported by NOAA,[7] one reason for the September 2019 extreme dryness in the SEUS was (with the exception of Hurricane Dorian along the Atlantic coast) the result of a lack of rain from tropical storms and hurricanes. The lack of landfalling storms indeed has a substantial impact on the total rainfall in the SEUS, especially during September, when tropical storms, on average, account for more than 20% of the total rainfall for that month (Knight and Davis 2007). We have shown here that those circulation anomalies appear to be tied to a Matsuno–Gill response to anomalous heating in the central/western tropical Pacific. We note that a similar Matsuno–Gill response, but centered over the tropical Atlantic, was found by Kucharski et al. (2009) to explain the influence of tropical Atlantic SST on summertime African and Indian monsoon rainfall.

The drought had no clear local precursor. August was characterized by near normal or slightly above-normal soil moisture conditions over much of the eastern United States, making it unlikely that preexisting local land conditions played a role. This is not inconsistent with the long-term trends, which show a nearly 40% increase in fall precipitation over the SEUS over the twentieth century (e.g., Bishop et al. 2019), with model projections indicating that anthropogenic climate change should enhance fall extreme (but not total) precipitation over the SEUS over the next century (Singh et al. 2013). In fact, as mentioned earlier, there is evidence for a step increase in fall precipitation in the eastern United States in the early 1970s linked to the emergence of a pan-Pacific Rossby wave train apparently forced by the increasing SST (and the associated deep convection) over the Indian Ocean (Strong et al. 2020).

In contrast, twentieth-century fall season temperature trends over the SEUS are not significant, and although model projections suggest we can expect future warming, some results indicate that the trends will be smallest over the SEUS (Kunkel et al. 2013). It would thus appear that regional trends in precipitation and temperature are unlikely to have contributed to the 2019 drought or to play a role in increasing the likelihood of such droughts in the future. This topic, however, requires further investigation, as changes in the frequency distribution of multiweek precipitation (as opposed to trends in mean precipitation)

[7] https://www.climate.gov/news-features/event-tracker/flash-drought-engulfs-us-southeast-september-2019.

are less well understood and are potentially more relevant for events similar to that in fall 2019 (e.g., Chen et al. 2020).

Given what we have learned about the causes of the drought, we turn now to the question: was this a freak event unlikely to recur in the near future? While we believe that we now have a good understanding of the various factors involved in producing the drought, we are less certain about their recurrence probabilities, so our overall assessment of whether or not similar droughts are imminent is, at this point, admittedly rather subjective. First, what are the chances of recurrence of the exact sequence of tropical forcing events that appear to have played such a key role in 2019? To the extent that there is a tendency for a positive IOD to follow El Niño events (e.g., Cai et al. 2012), we could argue that the sequence of events in which the drought is initiated by a Matsuno–Gill response to the SST remnants of a waning El Niño event, followed by the development of two Rossby waves (each forced by heating anomalies tied to a positive IOD), is not completely random. In fact, there is evidence of a causal link between the central Pacific El Niño that extended into the summer of 2019 and the subsequent development of the positive IOD (Doi et al. 2020). It is, however, still unclear how robust the links are between the IOD forcing and the exact phasing of the Rossby waves as they extend over North America. Is it simply a chance occurrence that the first wave amplified the drought while the second produced wet conditions over the SEUS? That may very well be the case.

Second, what about the future of the IOD? There appears to be a clear trend toward more frequent and strong positive IOD events in recent decades (Cai et al. 2009; see also Fig. 12). There is also theoretical work suggesting that the frequency of extreme positive IOD events may increase in response to greenhouse warming (Cai et al. 2014). As such, one can argue that we may expect more IOD-driven Rossby wave events to occur in the future. The exact regions impacted, and whether it is a short-term drought or flood, will depend on the exact phasing of the wave as it extends over North America. The lifetime of such drought or flood events is likely to be relatively short (perhaps a few weeks), tied to the lifetime of the Rossby waves, with land feedbacks potentially magnifying their amplitude (although we saw little evidence of that here; see the appendix). The fact that the 2019 SEUS drought persisted over a month, involving two, at best, weakly related forcing functions—the SST anomalies that developed in the tropical Pacific during the first two weeks of September, followed in late September and early October by SST anomalies that developed in the Indian Ocean associated with the IOD (together with the uncertainties about what determines the exact phasing of the Rossby waves over the SEUS)—makes it likely that the 2019 flash drought was indeed a freak event.

Finally, the fact that the free-running GEOS-5 AGCM (NORPL) was apparently unable to respond properly to the subseasonal fluctuations in the prescribed SST, both over the Indian Ocean (during the flash period and over the central/western tropical Pacific Ocean (during the inception period), requires more investigation. It may reflect deficiencies (including insufficient resolution) in the version of the GEOS-5 AGCM used here, or it may alternatively reflect limitations associated with forcing an uncoupled model with prescribed SST in regions where local coupled air–sea feedback is important (e.g., Wu and Kirtman 2004). We note that essentially the same GEOS-5 AGCM as that used here (but without TBC) has been used successfully in a number of studies addressing the responses to boreal cold season tropical SST forcing (e.g., Seager et al. 2015), indicating that the quality of the model's response to SST is well within the bounds of current state-of-the-art models. The importance of atmosphere–ocean coupling for the fall 2019 drought is supported by a look at recent subseasonal forecasts of this drought with the GEOS-5 coupled model (Molod et al. 2020); a preliminary analysis (not shown) suggests that, for short-term forecasts (1–2 weeks), the coupled model is capable of producing realistic precipitation anomalies in the tropics and realistic Rossby waves responses in the extratropics. Furthermore, lead one-month North American Multimodel Ensemble (NMME; Kirtman et al. 2014) forecasts (including the GEOS-5 coupled model) produced good predictions of the precipitation deficits over the SEUS for September 2019: a surprising result, given the historically poor skill of the NMME 1-month lead forecasts in the SE region for September.[8] This highlights the disadvantage of using average skill masks, and the need to improve our ability to assess forecast uncertainty in a way that allows us to better take advantage of forecasts of opportunity (Mariotti et al. 2020), as perhaps could have been done for this drought—this includes more research on what constitutes an adequate ensemble size for capturing extremes, especially on subseasonal time scales. Our results also point to the need to improve forecasts of tropical precipitation on subseasonal time scales as a critical step toward improving subseasonal forecasts of climate extremes over North America during the fall.

Acknowledgments. This work has been supported by the NASA MAP (NNG17HP01C) program and the NOAA Climate Program Office Modeling, Analysis, Prediction, and Projections (MAPP) program (NA14OAR4310221). MERRA-2 data were developed by the Global Modeling and Assimilation Office at NASA GSFC under funding by the NASA MAP program, and are disseminated through the Goddard Earth Science Data and Information Services Center (GES DISC). The 20th Century Reanalysis V3 data were provided by the NOAA/OAR/ESRL PSD, Boulder, Colorado, USA, from their web site at https://www.esrl.noaa.gov/psd/.

APPENDIX

Auxiliary Replay Experiments

As mentioned at the end of section 3c, understanding why RPL_TR reproduces the observed precipitation anomalies over the SEUS reasonably well, while RPL_IND does not, requires a closer look at the sensitivity of the results to the boundaries of the replay region and the potential interactions with the circulation in the other tropical ocean basins. To address that, we present here the results of several additional

[8] https://www.cpc.ncep.noaa.gov/products/NMME/archive/.

TABLE A1. List of auxiliary experiments. These differ from those discussed in the main text (Table 1) in the region being replayed and, in the case of RPL_TR_LND, in the treatment of the land surface. The blue lines in Fig. 1 outline the RPL_PAC and RPL_ATL regions.

Name	Time period	Initial conditions	Replay region	Ensemble members
RPL_TR_LND	1 Aug 2019–31 Dec 2019	RPL_TR	As in RPL_TR, but land conditions (temperature and soil moisture) over the globe are replaced by those from MERRA-2 every day at 2100 UTC starting 1 Aug 2019. Tropics (25°S–25°N)	30
RPL_TR_sub	30 Nov 2018–31 Dec 2019	MERRA-2	As in RPL_TR, but the northern boundary of the replay region is shifted south by 5° latitude east of the IND region (25°S–25°N, 0°–162°E; 25°S–20°N, 162°–360°E)	30
RPL_PAC	30 Nov 2018–31 Dec 2019	MERRA-2	Tropical Pacific (25°S–20°N, 162°–260°E)	30
RPL_ATL	30 Nov 2018–31 Dec 2019	MERRA-2	Tropical Atlantic (25°S–20°N, 260°–360°E)	30

replay experiments (see Table A1) that examine the sensitivity to the northern boundary of the tropical replay experiment (RPL_TR_sub) and the separate impacts of replaying the tropical Pacific (RPL_PAC) and Atlantic (RPL_ATL) regions. In the case of RPL_TR_sub we moved the northern boundary of the RPL_TR region (outside of the IND region) south by 5° latitude (see Fig. 1). This was done to help assess the extent to which the downstream impacts of the IND replay are controlled (simply by continuity) by the southern boundary. We also examine the impact of the land surface conditions (RPL_TR_LND). For those runs, the replay region is the same as that for RPL_TR, but the runs have the additional constraint that the model's predicted land conditions (temperature and soil moisture) are replaced every day by the actual values as estimated from MERRA-2. Those runs were initialized from the RPL_TR runs on 1 August 2019 (Table A1).

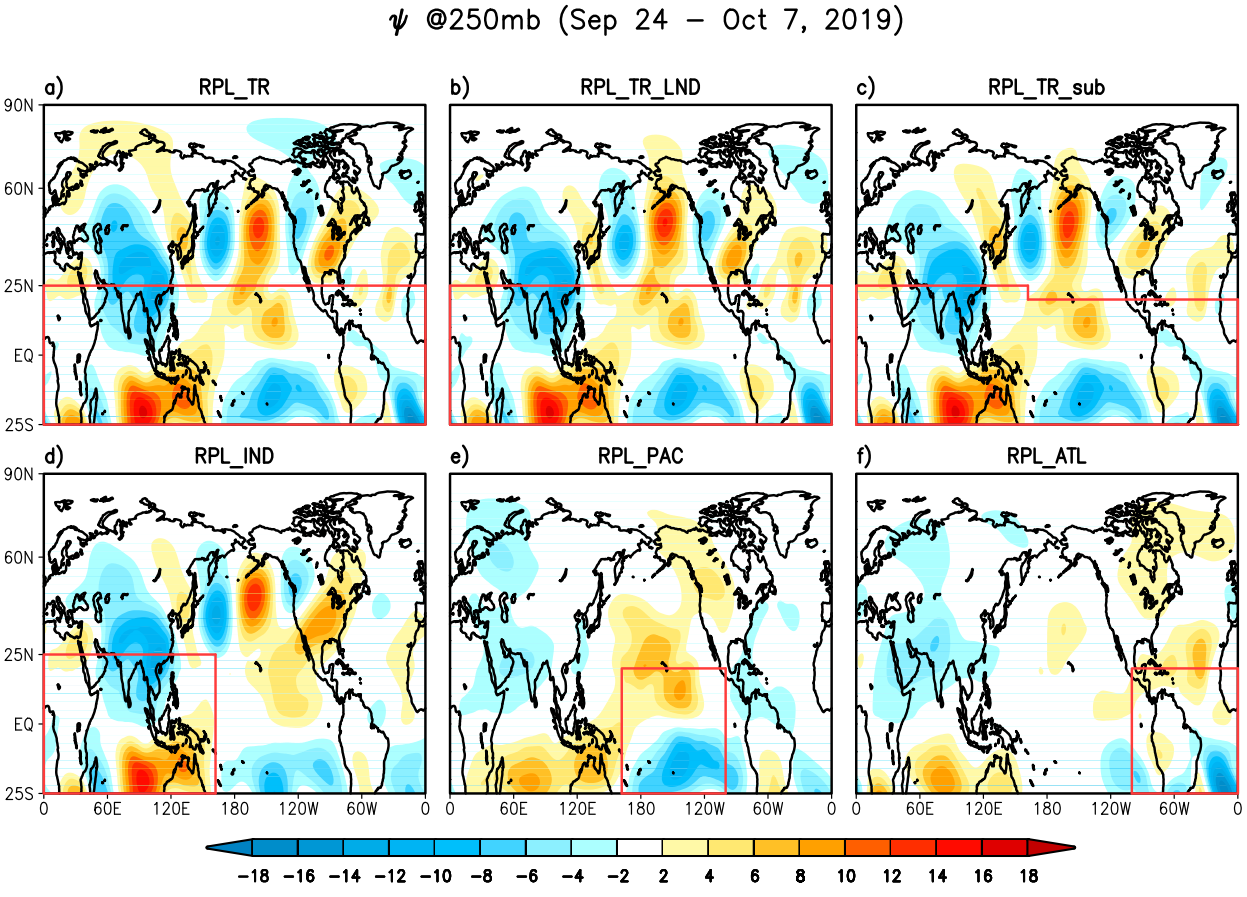

FIG. A1. The 250-mb eddy streamfunction anomalies (Ψ; $10^6\,m^2\,s^{-1}$) for (a) RPL_TR, (b) RPL_TR_LND, (c) RPL_TR_sub, (d) RPL_IND, (e) RPL_PAC, and (f) RPL_ATL averaged over the flash period 24 Sep–7 Oct 2019.

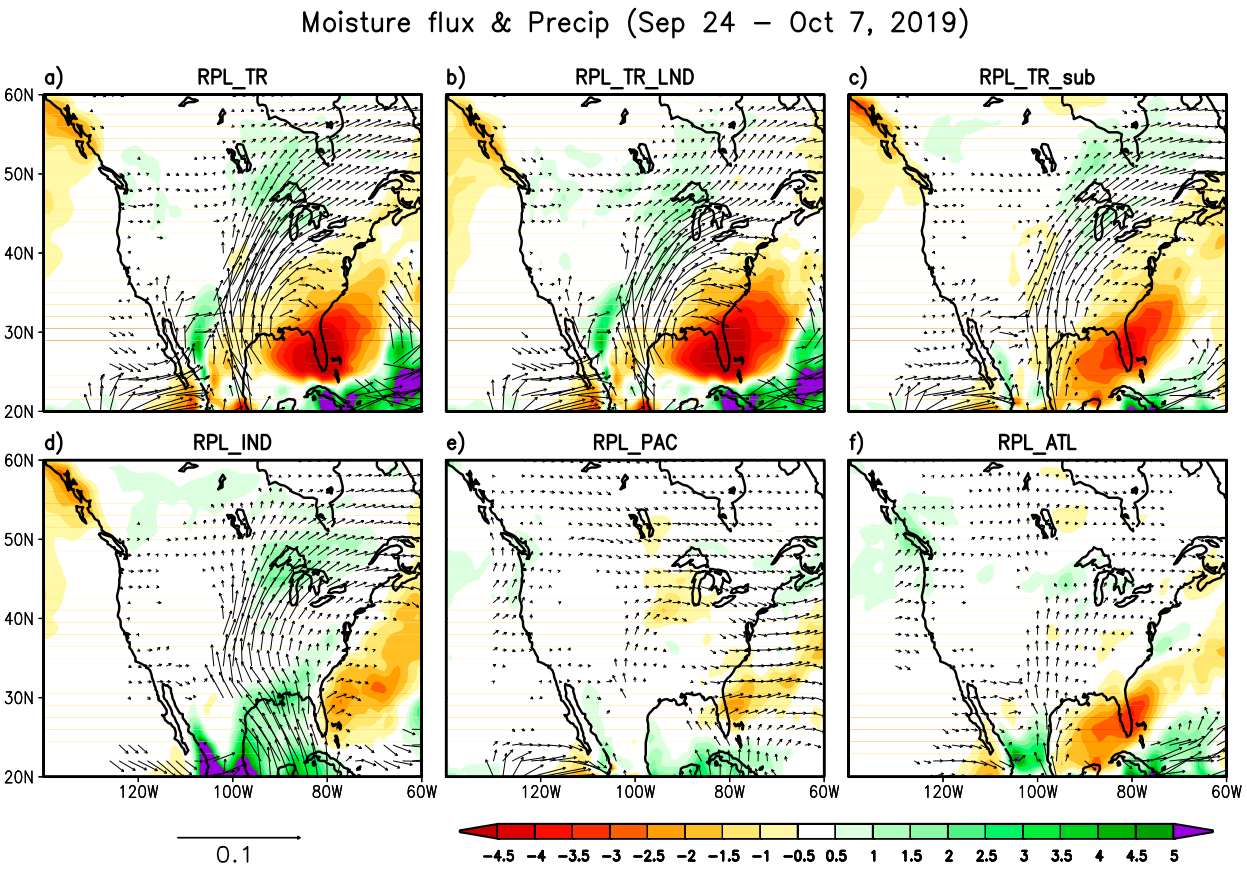

FIG. A2. The precipitation (shaded; mm day^{-1}) and 850-mb moisture flux anomalies (vectors; kg m s^{-1}) for (a) RPL_TR, (b) RPL_TR_LND, (c) RPL_TR_sub, (d) RPL_IND, (e) RPL_PAC, and (f) RPL_ATL averaged over the flash period 24 Sep–7 Oct 2019.

In the following, we focus on the flash period (24 September–7 October 2019) when the precipitation deficits over the SEUS are the most extreme, and we have argued that there is a strong link to a Rossby wave that originated in the IND region. Figure A1 shows the results for the 250-mb eddy streamfunction. We show here the streamfunction (rather than the height) anomalies to better resolve the connections with the tropics. The RPL_TR (Fig. A1a) again highlights the strong Rossby wave signature extending from the IND region across the North Pacific and North America with an anomalous ridge centered over the eastern United States. The results for RPL_TR_LND (Fig. A1b) show little impact of specifying the land conditions on the upper-level circulation. RPL_TR_sub (Fig. A1c) shows some impact on the wave train, especially over North America where the anomalous ridge over the eastern United States is weaker and shifted to the northwest (compared with RPL_TR), indicating some sensitivity of that ridge to the northern boundary of the replay region. The results for RPL_IND (Fig. A1d) again (as we saw in Fig. 5c) show the strong Rossby wave signature emanating from the IND region, with the maximum positive streamfunction anomaly over the eastern United States, broader and positioned farther to the south and west compared to that of RPL_TR. The impacts of RPL_PAC (Fig. A1e) and RPL_ATL (Fig. A1f) are quite different from RPL_IND, producing more localized impacts to the north of the replay regions, with RPL_PAC producing weak positive anomalies over western North America that could potentially impact the wave train emanating from the IND region, although the importance of this is unclear.

We next look at the precipitation and low-level moisture flux for these runs (Fig. A2). Comparing RPL_TR (Fig. A2a) with RPL_TR_LND (Fig. A2b), we see little impact on the dry conditions in the SE by specifying the land conditions, although with perhaps some strengthening of the positive precipitation anomalies in the middle of the country, making them more consistent with the MERRA-2 results in that region (cf. Fig. 6a). Comparing RPL_TR (Fig. A2a) with RPL_TR_sub (Fig. A2c), we see some reduction in the dry anomalies and the moisture fluxes in the SEUS, again reflecting some sensitivity of the results to the northern boundary of the RPL_TR region. Both RPL_PAC (Fig. A2e) and RPL_ATL (Fig. A2f) show generally weak moisture flux anomalies over the United States, yet RPL_ATL does contribute substantially to the dry anomalies over Florida. It is, however, unclear whether this represents an impact from the ATL region (Fig. 1) that is truly independent of the circulation anomalies produced by the Rossby wave train (emanating from the IND region) as it impinges on the Caribbean Sea and eastern tropical Atlantic (e.g., Fig. A1a). As such, we cannot separate out which, if any, of the

RPL_ATL results (and in particular the precipitation deficits over Florida) are truly independent of the Rossby wave impacts. The synchronization in time of the development of the Rossby wave and the development of the most extreme SEUS precipitation deficits during the flash period (see Fig. 2) would suggest a secondary independent impact from the ATL region. In any event, the above results highlight a limitation of the replay approach in parsing out the impacts of different regions of the globe, especially when those impacts overlap.

REFERENCES

Amaya, D. J., A. Miller, S. Xie, and Y. Kosaka, 2020: Physical drivers of the summer 2019 North Pacific marine heatwave. *Nat. Commun.*, **11**, 1903, https://doi.org/10.1038/S41467-020-15820-W.

Arcodia, M. C., B. P. Kirtman, and L. S. P. Siqueira, 2020: How MJO teleconnections and ENSO interference impact U.S. precipitation. *J. Climate*, **33**, 4621–4640, https://doi.org/10.1175/JCLI-D-19-0448.1.

Bishop, D. A., and Coauthors, 2019: Investigating the causes of increased twentieth-century fall precipitation over the southeastern United States. *J. Climate*, **32**, 575–590, https://doi.org/10.1175/JCLI-D-18-0244.1.

Cai, W., T. Cowan, and A. Sullivan, 2009: Recent unprecedented skewness towards positive Indian Ocean dipole occurrences and its impact on Australian rainfall. *Geophys. Res. Lett.*, **36**, L11705, https://doi.org/10.1029/2009GL037604.

——, P. van Rensch, T. Cowan, and H. H. Hendon, 2012: An asymmetry in the IOD and ENSO teleconnection pathway and its impact on Australian climate. *J. Climate*, **25**, 6318–6329, https://doi.org/10.1175/JCLI-D-11-00501.1.

——, and Coauthors, 2014: Increased frequency of extreme Indian Ocean dipole events due to greenhouse warming. *Nature*, **510**, 254–258, https://doi.org/10.1038/nature13327.

Chang, Y., S. D. Schubert, R. D. Koster, A. M. Molod, and H. Wang, 2019: Tendency bias correction in coupled and uncoupled global climate models with a focus on impacts over North America. *J. Climate*, **32**, 639–661, https://doi.org/10.1175/JCLI-D-18-0598.1.

Chen, H., S. Wang, and Y. Wang, 2020: Exploring abrupt alternations between wet and dry conditions on the basis of historical observations and convection-permitting climate model simulations. *J. Geophy. Res. Atmos.*, **125**, e2019JD031982, https://doi.org/10.1029/2019JD031982.

DeAngelis, A. M., H. Wang, R. D. Koster, S. D. Schubert, Y. Chang, and J. Marshak, 2020: Prediction skill of the 2012 U.S. Great Plains flash drought in subseasonal experiment (SubX) models. *J. Climate*, **33**, 6229–6253, https://doi.org/10.1175/JCLI-D-19-0863.1.

Doi, T., S.K. Behera, and T. Yamagata, 2020: Predictability of the super IOD event in 2019 and its link with El Niño Modoki. *Geophys. Res. Lett.*, **47**, e2019GL086713, https://doi.org/10.1029/2019GL086713.

Gelaro, R., and Coauthors, 2017: The Modern-Era Retrospective Analysis for Research and Applications, version 2 (MERRA-2). *J. Climate*, **30**, 5419–5454, https://doi.org/10.1175/JCLI-D-16-0758.1.

Gill, A. E., 1980: Some simple solutions for heat-induced tropical circulations. *Quart. J. Roy. Meteor. Soc.*, **106**, 447–462, https://doi.org/10.1002/qj.49710644905.

Hoerling, M., J. Eischeid, A. Kumar, R. Leung, A. Mariotti, K. Mo, S. Schubert, and R. Seager, 2014: Causes and predictability of the 2012 Great Plains drought. *Bull. Amer. Meteor. Soc.*, **95**, 269–282, https://doi.org/10.1175/BAMS-D-13-00055.1.

Ihara, C., Y. Kushnir, and M. Cane, 2008: Warming trend of the Indian Ocean SST and Indian Ocean dipole from 1880 to 2004. *J. Climate*, **21**, 2035–2046, https://doi.org/10.1175/2007JCLI1945.1.

Kirtman, B. P., and Coauthors, 2014: The North American multimodel ensemble: Phase-1 seasonal-to-interannual prediction: Phase-2 toward developing intraseasonal prediction. *Bull. Amer. Meteor. Soc.*, **95**, 585–601, https://doi.org/10.1175/BAMS-D-12-00050.1.

Knight, D. B., and R. E. Davis, 2007: Climatology of tropical cyclone rainfall in the southeastern United States. *Phys. Geogr.*, **28**, 126–147, https://doi.org/10.2747/0272-3646.28.2.126.

Koster, R. D., Y. Chang, and S. D. Schubert, 2014: A mechanism for land–atmosphere feedback involving planetary wave structures. *J. Climate*, **27**, 9290–9301, https://doi.org/10.1175/JCLI-D-14-00315.1.

Kucharski, F., A. Bracco, J. H. Yoo, A. M. Tompkins, L. Feudale, P. M. Ruti, and A. Dell'Aquila, 2009: A Gill–Matsuno-type mechanism explains the tropical Atlantic influence on African and Indian monsoon rainfall. *Quart. J. Roy. Meteor. Soc.*, **135**, 569–579, https://doi.org/10.1002/qj.406.

Kunkel, K., and Coauthors, 2013: Regional climate trends and scenarios for the US National Climate Assessment: Part 4. Climate of the U.S. Great Plains. NOAA Tech. Rep. NESDIS 142–4, 82 pp., https://scenarios.globalchange.gov/sites/default/files/NCA-GP_Regional_Scenario_Summary_20130517_banner.pdf.

Lindzen, R. S., and S. Nigam, 1987: On the role of sea surface temperature gradients in forcing low-level winds and convergence in the tropics. *J. Atmos. Sci.*, **44**, 2418–2436, https://doi.org/10.1175/1520-0469(1987)044<2418:OTROSS>2.0.CO;2.

Mariotti, A., and Coauthors, 2020: Windows of opportunity for skillful forecasts subseasonal to seasonal and beyond. *Bull. Amer. Meteor. Soc.*, **101**, E608–E625, https://doi.org/10.1175/BAMS-D-18-0326.1.

Matsuno, T., 1966: Quasi-geostrophic motions in the equatorial area. *J. Meteor. Soc. Japan*, **44**, 25–43, https://doi.org/10.2151/jmsj1965.44.1_25.

Menkes, C. E., J. G. Vialard, S. C. Kennan, J. Boulanger, and G. V. Madec, 2006: A modeling study of the impact of tropical instability waves on the heat budget of the eastern equatorial Pacific. *J. Phys. Oceanogr.*, **36**, 847–865, https://doi.org/10.1175/JPO2904.1.

Molod, A., L. Takacs, M. Suarez, and J. Bacmeister, 2015: Development of the GEOS-5 atmospheric general circulation model: Evolution from MERRA to MERRA2. *Geosci. Model Dev.*, **8**, 1339–1356, https://doi.org/10.5194/gmd-8-1339-2015.

——, and Coauthors, 2020: GEOS-S2S version 2: The GMAO high-resolution coupled model and assimilation system for seasonal prediction. *J. Geophys. Res. Atmos.*, **125**, e2019JD031767, https://doi.org/10.1029/2019JD031767.

Nigam, S., B. Guan, and A. Ruiz-Barradas, 2011: Key role of the Atlantic Multidecadal Oscillation in 20th century drought and wet periods over the Great Plains. *Geophys. Res. Lett.*, **38**, L16713, https://doi.org/10.1029/2011GL048650.

Park Williams, A., B. I. Cook, J. E. Smerdon, D. A. Bishop, R. Seager, and J. S. Mankin, 2017: The 2016 southeastern U.S. drought: An extreme departure from centennial wetting and cooling. *J. Geophys. Res. Atmos.*, **122**, 102888–102905, https://doi.org/10.1002/2017JD027523.

Reichle, R. H., R. D. Koster, G. J. M. De Lannoy, B. A. Forman, Q. Liu, S. P. P. Mahanama, and A. Toure, 2011: Assessment and enhancement of MERRA land surface hydrology estimates. *J. Climate*, **24**, 6322–6338, https://doi.org/10.1175/JCLI-D-10-05033.1.

Saji, N. H., B. N. Goswami, P. N. Vinayachandran, and T. Yamagata, 1999: A dipole mode in the tropical Indian Ocean. *Nature*, **401**, 360–363, https://doi.org/10.1038/43854.

Schubert, S., H. Wang, and M. Suarez, 2011: Warm season subseasonal variability and climate extremes in the Northern Hemisphere: The role of stationary Rossby waves. *J. Climate*, **24**, 4773–4792, https://doi.org/10.1175/JCLI-D-10-05035.1.

——, A. Borovikov, Y.-K. Lim, and A. Molod, 2019a: Ensemble generation strategies employed in the GMAO GEOS-S2S forecast system, Tech. Rep. Series on Global Modeling and Data Assimilation, R. D. Koster, Ed., NASA/TM-2019-104606, Vol. 53, 65 pp.

——, Y. Chang, H. Wang, R. D. Koster, and A. M. Molod, 2019b: A systematic approach to assessing the sources and global impacts of errors in climate models. *J. Climate*, **32**, 8301–8321, https://doi.org/10.1175/JCLI-D-19-0189.1.

Seager, R., and M. Hoerling, 2014: Atmosphere and ocean origins of North American droughts. *J. Climate*, **27**, 4581–4606, https://doi.org/10.1175/JCLI-D-13-00329.1.

——, ——, S. Schubert, H. Wang, B. Lyon, A. Kumar, J. Nakamura, and N. Henderson, 2015: Causes of the 2011–14 California drought. *J. Climate*, **28**, 6997–7024, https://doi.org/10.1175/JCLI-D-14-00860.1.

Showman, A., and L. Polvani, 2010: The Matsuno–Gill model and equatorial superrotation. *Geophys. Res. Lett.*, **37**, L18811, https://doi.org/10.1029/2010GL044343.

Singh, D., M. Tsiang, B. Rajaratnam, and N. S. Diffenbaugh, 2013: Precipitation extremes over the continental United States in a transient, high-resolution, ensemble climate model experiment. *J. Geophys. Res. Atmos.*, **118**, 7063–7086, https://doi.org/10.1002/jgrd.50543.

Slivinski, L. C., and Coauthors, 2019: Towards a more reliable historical reanalysis: Improvements for version 3 of the Twentieth Century Reanalysis system. *Quart. J. Roy. Meteor. Soc.*, **145**, 2876–2908, https://doi.org/10.1002/qj.3598.

Strong, C., G. J. McCabe, and A. Weech, 2020: Step increase in eastern U.S. precipitation linked to Indian Ocean warming. *Geophys. Res. Lett.*, **47**, e2020GL088911, https://doi.org/10.1029/2020GL088911.

Ting, M. F., and L. Yu, 1998: Steady response to tropical heating in wavy linear and nonlinear baroclinic models. *J. Atmos. Sci.*, **55**, 3565–3582, https://doi.org/10.1175/1520-0469(1998)055<3565:SRTTHI>2.0.CO;2.

Wang, H., S. Schubert, R. Koster, Y. Ham, and M. Suarez, 2014: On the role of SST forcing in the 2011 and 2012 extreme U.S. heat and drought: A study in contrasts. *J. Hydrometeor.*, **15**, 1255–1273, https://doi.org/10.1175/JHM-D-13-069.1.

——, ——, ——, and Y. Chang, 2019: Phase locking of the boreal summer atmospheric response to dry land surface anomalies in the Northern Hemisphere. *J. Climate*, **32**, 1081–1099, https://doi.org/10.1175/JCLI-D-18-0240.1.

Webster, P. J., A. M. Moore, J. P. Loschnigg, and R. R. Leben, 1999: Coupled ocean–atmosphere dynamics in the Indian Ocean during 1997–98. *Nature*, **401**, 356–360, https://doi.org/10.1038/43848.

Wheeler, M. C., and H. H. Hendon, 2004: An all-season real-time multivariate MJO index: Development of an index for monitoring and prediction. *Mon. Wea. Rev.*, **132**, 1917–1932, https://doi.org/10.1175/1520-0493(2004)132,1917:AARMMI.2.0.CO;2.

Wu, R., and B. P. Kirtman, 2004: Impacts of the Indian Ocean on the Indian summer monsoon–ENSO relationship. *J. Climate*, **17**, 3037–3054, https://doi.org/10.1175/1520-0442(2004)017<3037:IOTIOO>.0.CO;2.